

On the Achievability of Submeter-Accurate UAV Navigation With Cellular Signals Exploiting Loose Network Synchronization

JOE KHALIFE , Member, IEEE

ZAHER M. KASSAS , Senior Member, IEEE
University of California, Irvine, CA USA

A framework that could achieve submeter-level unmanned aerial vehicle (UAV) horizontal navigation in multipath-free environments with cellular carrier phase measurements is developed. This framework exploits the “loose” synchronization between cellular base transceiver station (BTS) clocks. It is shown through extensive experimental data that the beat frequency stability of cellular BTSs approaches that of atomic standards and that the clock deviations can be realized as a stable autoregressive moving average model. This BTS clock model is referred to as loose network synchronization. A rule-of-thumb is established for clustering the clock deviations to minimize the position estimation error, while significantly reducing the computational complexity. The presented models allow the UAV to achieve sustained carrier phase-based meter- to submeter-accurate navigation. To demonstrate the efficacy of the developed framework, this article presents three UAV flight experiments in Southern California, USA, utilizing signals from different cellular providers transmitting at different frequencies. The three experiments took place in open, semiurban environments with nearly multipath-free, line-of-sight (LOS) conditions, in which the UAV traveled 1.72, 3.07, and 0.61 km, achieving a horizontal position root mean squared error of 36.61, 88.58, and 89.33 cm, respectively, with respect to the UAV’s on-board navigation system.

Manuscript received 19 January 2022; released for publication 11 March 2022. Date of publication 31 March 2022; date of current version 11 October 2022.

DOI. No. 10.1109/TAES.2022.3162770

Refereeing of this contribution was handled by S. Khanafseh.

This work was supported in part by the Office of Naval Research (ONR) under Grant N00014-16-1-2305 and Grant N00014-19-1-2511 and in part by the U.S. Department of Transportation (USDOT) under Grant 69A3552047138 for the CARMEN University Transportation Center (UTC).

Authors’ addresses: The authors are with the Department of Mechanical and Aerospace Engineering, University of California, Irvine, CA 92617 USA, E-mail: (jkkhalife@gmail.com; zkassas@ieee.org). (Corresponding author: Zaher M. Kassas.)

0018-9251 © 2022 IEEE

I. INTRODUCTION

Unmanned aerial vehicles (UAVs) will demand a resilient, accurate, and tamper-proof navigation system [1]. Current UAV navigation systems will not meet these stringent demands as they are dependent on global navigation satellite system (GNSS) signals, which are jammable, spoofable, and may not be usable in certain environments (e.g., deep urban canyons) [2]–[4]. The potential of signals of opportunity (SOPs) (e.g., AM/FM radio [5]–[7], low Earth orbit (LEO) satellite [8]–[12], Wi-Fi [13]–[16], digital television [17]–[21], and cellular [22]–[32]) as complementary or alternative navigation sources have been the subject of extensive research recently. Navigation with SOPs has been demonstrated on ground vehicles and UAVs, achieving a localization accuracy ranging from meters to tens of meters, with the latter accuracy corresponding to ground vehicles in deep urban canyons with severe multipath conditions [33]–[39]. Cellular signals, particularly 3G code-division multiple access (CDMA), 4G long-term evolution (LTE), and 5G new radio (NR), are among the most attractive SOP candidates for navigation. These signals are abundant, received at a much higher power than GNSS signals, offer a favorable horizontal geometry, and are free to use. Unlike ultra-wide bandwidth positioning [40], [41], cellular SOP-based navigation does not require additional transmitter infrastructure. Several receiver designs have been proposed recently that produce navigation observables from cellular CDMA, LTE, and NR signals [23], [42]–[45]. Moreover, error sources pertaining to code phase-based navigation with cellular CDMA systems have been derived and performance under such errors has been characterized [24], [44]. While cellular signals are jammable and spoofable [46]–[49], they are typically received outdoors at carrier-to-noise ratios that are more than 30 dB higher than GNSS signals [50]. As such, considerably higher power would be needed to jam cellular signals than is needed to jam GNSS signals. Moreover, cellular signals are transmitted in multiple frequency bands. The cellular 3G, 4G, and 5G spectrum spans the 700 MHz to nearly 6 GHz bands. The 5G millimeter wave (mmWave) spectrum is envisioned to span several GHz of spectrum, with some bands reaching up to 400 MHz of bandwidth. Unless most cellular bands are simultaneously attacked, an SOP receiver could detect the attack by leveraging redundancy in the measurements. This makes staging a successful, clandestine attack on cellular SOPs generally challenging, as the attacker would need to target the entire cellular spectrum. Although not impossible, the capability of completely jamming cellular SOPs has not become as accessible yet as in the case of jamming GNSS signals, which can be readily performed through illegal but widely available personal privacy devices. As jamming technology becomes more capable, navigation systems can be made more robust by exploiting more signals, whether dedicated navigation signals or other forms of SOPs.

A challenge that arises in cellular-based navigation is the unknown states of cellular base transceiver stations (BTSs), namely their position and clock errors (bias and drift).

This is in sharp contrast to GNSS-based navigation, where the states of the satellites are transmitted to the receiver in the navigation message. To deal with this challenge, a base/rover framework was proposed in [24], [44], [51], in which the base and rover make pseudorange measurements to the same BTSs in the environment. The base was assumed to have complete knowledge of its states (e.g., by having access to GNSS signals), while estimating the states of BTSs in its environment, and sharing these estimates with a rover that had no knowledge of its states. Another framework was developed in which the rover estimated its states simultaneously with the states of the BTSs in the environment, i.e., performed radio simultaneous localization and mapping (radio SLAM) [52]–[55]. It is worth noting that since cellular BTSs are spatially stationary, their positions may be mapped prior to navigation (e.g., by dedicated mapping receivers [56] or from satellite imagery and cellular databases). However, the BTSs’ clocks errors must be continuously estimated, whether in the base/rover framework or radio SLAM framework, since these errors are stochastic and dynamic.

A preliminary study for cellular carrier phase-based nondifferential single UAV navigation was conducted in [25]. The proposed framework relied on the relative stability of 3G CDMA cellular BTS clocks. It was revealed that while these clocks are not perfectly synchronized to GNSS, the clock biases of different neighboring BTSs are dominated by a common term. Another study was conducted for 4G LTE cellular BTSs, also known as eNBs, in the presence of real GPS jamming [57]. The study showed that LTE eNBs maintain tight synchronization for at least 90 min, even in the absence of GPS signals. These key findings suggest that precise carrier phase navigation with cellular signals is achievable with or without a base.

This article presents a comprehensive study in which a UAV navigating using cellular carrier phase measurements could achieve submeter-level accuracy in a multipath-free environment with line-of-sight (LOS) conditions. It is assumed that the UAV has knowledge of its position for a period of time, e.g., from a GNSS receiver or from the cellular-based differential framework proposed in [51], before loss of communication with the base, whether initially or intermittently. It is important to note that the algorithms presented in this article are agnostic to the cellular signal type (3G, 4G, 5G, and beyond) as long as navigation observables can be produced from these signals. This article studies 3G and 4G signals and the carrier phase observables were obtained using the receivers proposed in [23] and [44]. The proposed framework assumes a certain level of synchronization between the towers, which has been observed in 3G and 4G systems [25], [57]. This article shows that while cellular networks are not as tightly synchronized as GPS, since they are not intended for navigation, there are strong correlations between the BTS clock biases. This level of synchronization is referred to as “loose” network synchronization. A clock bias clustering algorithm is developed, motivated by the strong correlations between the clock biases. This results in a tradeoff between 1) lost accuracy due to eliminating

some clock biases and 2) improved precision by reducing the dilution of precision (DOP). The proposed clustering method aims at exploiting the correlations between BTS clock biases to resolve this tradeoff by minimizing the resulting position error. In particular, this article extends [25] by making the following three contributions:

- 1) A comprehensive method to obtain the statistics of the BTS clock deviations is presented. It is shown that the beat frequency stability of cellular BTSs approaches that of atomic standards and that the clock deviations can be realized as a stable autoregressive moving average (ARMA) model. The stationarity of such deviations is validated experimentally.
- 2) The navigation performance is analyzed extensively as a function of clustering frequency.
- 3) Extensive experimental results with 3G CDMA and 4G LTE signals from different cellular providers transmitting at different frequencies are presented, demonstrating the efficacy of the proposed framework. The UAV flight experiments took place in Southern California, USA, in three different open semiurban environments with multipath-free LOS conditions. In all experiments, the UAV remained within the same sector of each BTS. The UAV achieved a horizontal position root mean-squared error (RMSE) of: 1) 36.61 cm over a trajectory of 1.72 km, 2) 88.58 cm over a trajectory of 3.07 km, and 3) 89.33 cm over a trajectory of 609 m. The RMSEs were calculated relative to the UAV’s on-board navigation solution.

The rest of this article is organized as follows. Section II describes the cellular carrier phase observable model. Section III describes the single-UAV navigation framework that leverages the relative stability of cellular SOPs. Section IV provides experimental results demonstrating the proposed framework, showing submeter-level UAV navigation accuracy in nearly multipath-free environments. Finally, Section V concludes this article.

II. CELLULAR CARRIER PHASE OBSERVABLE MODEL

In cellular systems, several known signals are transmitted for synchronization or channel estimation purposes. In cellular CDMA systems, a pilot signal consisting of a pseudorandom noise sequence, known as the short code, is modulated by a carrier signal and broadcast by each BTS for synchronization purposes [58]. Therefore, by knowing the shortcode, the receiver may measure the code phase of the pilot signal as well as its carrier phase; hence, forming a pseudorange measurement to each BTS transmitting the pilot signal. In LTE, two synchronization signals [primary synchronization signal (PSS) and secondary synchronization signal (SSS)] are broadcast by each BTS, referred to evolved node B (eNodeB) in LTE systems [59]. In addition to the PSS and SSS, a reference signal known as the cell-specific reference signal (CRS), is transmitted by each eNodeB for channel estimation purposes [59]. The PSS,

SSS, and CRS may be exploited to draw carrier phase and pseudorange measurements on neighboring eNodeBs [23], [37]. In the rest of this article, availability of code phase, Doppler frequency, and carrier phase measurements of cellular CDMA and LTE signals is assumed (e.g., from specialized navigation receivers [23], [35], [37], [42]–[44], [60]).

Let $n \in \{1, \dots, N\}$ denote the cellular SOP index, where N is the total number of SOPs. Moreover, let $k = 0, 1, \dots$, denote the time index, which represents time at $t_k = t_0 + kT$, where t_0 is some initial time and T is the subaccumulation period in the receiver. The carrier phase at time-step k , expressed in meters, can be parameterized in terms of the receiver and cellular SOP states as

$$z_n(k) = \sqrt{\|\mathbf{r}_r(k) - \mathbf{r}_{s_n}\|_2^2 + \Delta z_{r,s_n}^2(k)} + c \cdot [\delta t_r(k) - \delta t_{s_n}(k)] + \lambda N_n + v_n(k) \quad (1)$$

where $\mathbf{r}_r \triangleq [x_r, y_r]^T$ is the receiver's two-dimensional (2-D) position vector; $\mathbf{r}_{s_n} \triangleq [x_{s_n}, y_{s_n}]^T$ is the cellular BTS's known 2-D position vector; $\Delta z_{r,s_n} \triangleq z_r(k) - z_{s_n}$ is the difference between the receiver' and BTS's altitude; c is the speed of light; δt_r and δt_{s_n} are the receiver's and cellular BTS's clock biases, respectively; λ is the signal's wavelength; N_n is the carrier phase ambiguity; and $v_n(k)$ is the measurement noise, which is modeled as a discrete-time zero-mean white Gaussian sequence with variance $\sigma_n^2(k)$. Note that a coherent phase-locked loop (PLL) may be employed in CDMA and LTE navigation receivers, since the cellular synchronization and reference signals do not carry any data. As such, the measurement noise variance can be expressed as [61]

$$\sigma_n^2(k) = \lambda^2 \frac{B_{\text{PLL}}}{C/N_{0,n}(k)} \quad (2)$$

where B_{PLL} is the receiver's PLL noise equivalent bandwidth and $C/N_{0,n}(k)$ is the cellular SOP's measured carrier-to-noise ratio at time-step k . The remainder of this article assumes zero-mean Gaussian measurement noise. The actual measurement noise statistics may differ from the what is assumed in (2). Therefore, instead of using (2), Gaussian overbounds of the true measurement noise distribution could be used, if known. Methods described in [62]–[64] could be used to compute overbounds of the measurement noise statistics in different environments. Note that small UAVs and hearable cellular BTSs are typically at comparable altitudes, which makes the vertical diversity very poor. Therefore, one can only estimate the UAV's horizontal position using cellular SOPs without introducing significant errors. As such, the proposed frameworks assume that the UAV and BTS altitudes, $z_r(k)$ and z_{s_n} , respectively, are known and only the UAV's 2–D position is estimated.

It is important to note that the channels between the UAVs and the cellular BTSs do not suffer from severe multipath, as a strong LOS component is usually observed in the received signal [65]. In the case of severe multipath or non-LOS (NLOS) conditions, it is assumed that either 1) signal processing techniques at the SOP receiver level [37],

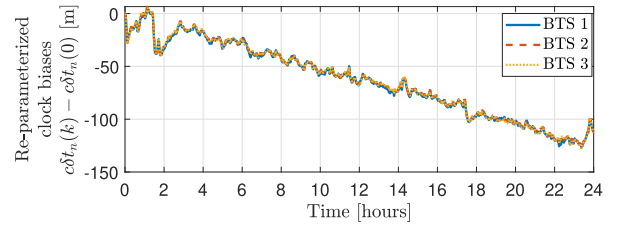


Fig. 1. Experimental data showing $c\delta t_n(k) - c\delta t_n(0)$ obtained from carrier phase measurements over 24 hours for three neighboring BTSs. It can be seen that the clock biases $c\delta t_n(k)$ in the carrier phase measurement are very similar, up to an initial bias $c\delta t_n(0)$ which has been removed.

Remark: The receiver's clock was derived from a GPS-disciplined oven-controlled crystal oscillator (OCXO), which do not typically have a long-term drift. Therefore, the observed drift is most likely due to the BTS clocks. However, this does not affect the new clock model as it does not disambiguate between the BTS and receiver clock biases and only considers their difference, as per (11).

[66]–[72] or 2) measurement outlier rejection techniques [62] are used to mitigate multipath or exclude measurements with large errors due to multipath. Concepts of receiver autonomous integrity monitoring may also be used to exclude measurements with large errors, which can be considered as faulty measurements [73]–[75]. Alternatively, multipath error models may be used to predict and mitigate large measurement errors, either through multipath prediction maps [63], [76] or statistical models [77]. To this end, it is assumed in the rest of this article that the effect of multipath has either 1) been mitigated or 2) included in the measurement model (1).

III. PRECISE NAVIGATION WITH SOP CARRIER PHASE MEASUREMENTS

This section discusses a cellular carrier phase navigation framework that is employable on a single UAV.

A. Combined Clock Errors

The terms $c[\delta t_r(k) - \delta t_{s_n}(k) + \frac{\lambda}{c}N_n]$ are not needed to be estimated individually and are thus combined into one term defined as

$$c\delta t_n(k) \triangleq c \left[\delta t_r(k) - \delta t_{s_n}(k) + \frac{\lambda}{c}N_n \right]. \quad (3)$$

The combined clock errors of three BTSs over a 24-h period are shown in Fig. 1. It was noted in [78] that while large differences between the BTSs' clock biases may be observed (the code phase synchronization requirement as per the cellular protocol is to be within $3 \mu\text{s}$), cellular BTSs possess tight carrier frequency synchronization, as seen by the Allan deviations computed for the three BTSs over 24 h and shown in Fig. 2. Therefore, the resulting clock biases in the carrier phase estimates will be very similar, up to an initial bias, as shown in Fig. 1. This level of synchronization is referred to as loose network synchronization. Consequently, one may leverage this relative frequency stability to eliminate parameters that need to be estimated. Moreover, this allows one to use a static estimator (e.g., a WNLS) to estimate the position of the UAV. To achieve this, in what follows,

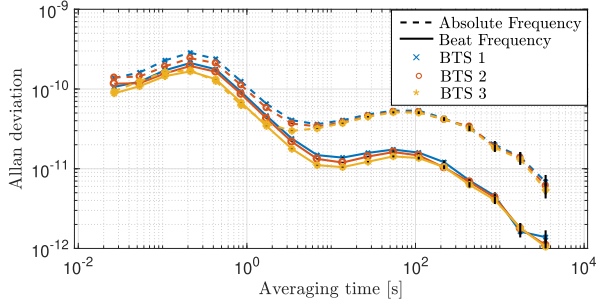


Fig. 2. Allan deviations of absolute and beat frequencies for the 3 BTSs shown in Fig. 1. The beat frequency is calculated from the clock drift between two BTSs, whereas the absolute frequency is the clock drift between the receiver and BTS. The Allan deviations were calculated from data collected over 24 h. The carrier frequency was 883.98 MHz. It is worth noting that while the beat frequency stability approaches that of atomic standards, it is not quite the same as it tends upwards for relatively short averaging periods of 0.1 to 100 s. This could be due to the fact that GPS corrections on the BTSs' clocks happen gradually over several seconds.

the carrier phase measurement is first reparameterized and a WNLS estimation framework is subsequently developed. In what follows, it is assumed that the UAV remains within one sector of a particular BTS. A complete treatment of clock bias mismatches arising due to crossing BTS sectors is discussed in [24] and [44].

B. Carrier Phase Measurement Reparametrization

Motivated by the experimental results in [78], the following reparametrization is proposed

$$c\bar{\delta}t_n(k) \triangleq c\delta t_n(k) - c\delta t_n(0) \equiv c\delta t(k) + \epsilon_n(k) \quad (4)$$

where $c\delta t$ is a time-varying common bias term and ϵ_n is the deviation of $c\bar{\delta}t_n$ from this common bias and is treated as measurement noise. Using (4), the carrier phase measurement (1) can be reparameterized as

$$z_n(k) = \sqrt{\|\mathbf{r}_r(k) - \mathbf{r}_{s_n}\|_2^2 + \Delta z_{r,s_n}^2} + c\delta t(k) + c\delta t_{0_n} + \eta_n(k) \quad (5)$$

where $c\delta t_{0_n} \triangleq c\delta t_n(0)$ and $\eta_n(k) \triangleq \epsilon_n(k) + v_n(k)$ is the overall measurement noise. The statistics of ϵ_n will be discussed in Section III-E. Note that $c\delta t_{0_n}$ can be obtained knowing the initial position and given the initial measurement $z_n(0)$ according to $c\delta t_{0_n} \approx z_n(0) - \sqrt{\|\mathbf{r}_r(0) - \mathbf{r}_{s_n}\|_2^2 + \Delta z_{r,s_n}^2(0)}$. This approximation ignores the contribution of the initial measurement noise. If the receiver is initially stationary for a period k_0T seconds, which is short enough such that $\delta t(k) \approx 0$ for $k = 1, \dots, k_0$, then the first k_0 samples may be averaged to obtain a more accurate estimate of $c\delta t_{0_n}$.

It is proposed that instead of lumping all N clock biases into one bias $c\delta t$ to be estimated, the clocks get clustered into L clusters, each of size N_l such as

$$\sum_{l=1}^L N_l = N. \quad (6)$$

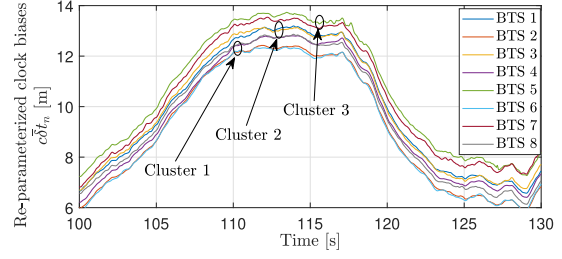


Fig. 3. Experimental data for re-parameterized clock biases $c\bar{\delta}t_n(k)$ over 30 s for 8 BTSs. The clock biases have been visually clustered into three clusters as an illustrative example.

As such, the clocks in a cluster l are lumped into one bias $c\delta t_l$ to be estimated. This gives finer granularity for the parametrization (4), since naturally, certain groups of cellular SOPs will be more synchronized with each other than with other groups (e.g., corresponding to the same network provider, transmission protocol, etc.) or some may lose synchronization altogether in some unlikely event. In the case of complete loss of synchronization, a framework for navigation with asynchronous SOPs could be used instead at the price of lower position accuracy [79]. An illustrative experimental plot is shown in Fig. 3. The figure shows an oscillating, dominant common term that is most likely due to the receiver's clock bias. Note that since the 2-D position vector of the UAV is being estimated along with L clock biases, the number of clusters L cannot exceed $N - 2$, otherwise there would be more unknowns than measurements.

Without loss of generality, it is assumed that the carrier phase measurements have been ordered such that the first N_1 measurements were grouped into the first cluster, the second N_2 measurements were grouped into the second cluster, et. Next, obtaining the navigation solution with a WNLS is discussed.

C. Navigation Solution

Given $N \geq 3$ pseudoranges modeled according to (5) and $L \leq N - 2$ SOP clusters, the receiver may solve for its current position \mathbf{r}_r and the current set of common biases $c\delta t \triangleq [c\delta t_1, \dots, c\delta t_L]^T$ using a WNLS estimator. The state to be estimated is defined by $\mathbf{x} \triangleq [\mathbf{r}_r^T, c\delta t^T]^T$. An estimate $\hat{\mathbf{x}}$ may be obtained using the iterated WNLS equations as

$$\hat{\mathbf{x}}^{(j+1)}(k) = \hat{\mathbf{x}}^{(j)}(k) + (\mathbf{H}^T \mathbf{R}_\eta^{-1} \mathbf{H})^{-1} \mathbf{H}^T \mathbf{R}_\eta^{-1} \delta \mathbf{z}(k) \quad (7)$$

where $\delta \mathbf{z}(k) \triangleq [\delta z_1(k), \dots, \delta z_N(k)]^T$ and $\delta z_n(k) \triangleq z_n(k) - \left[\sqrt{\|\hat{\mathbf{r}}_r^{(j)}(k) - \mathbf{r}_{s_n}\|_2^2 + \Delta z_{r,s_n}^2(k)} + c\delta t_{l(n)}^{(j)}(k) + c\delta t_{0_n} \right]$, $\mathbf{R}_\eta = \text{diag}[\sigma_1^2 + \sigma_{\epsilon_1}^2, \dots, \sigma_N^2 + \sigma_{\epsilon_N}^2]$ is the measurement noise covariance, where $\sigma_{\epsilon_n}^2$ will be discussed in Section III-E, j is the WNLS iteration index, and \mathbf{H} is the measurement Jacobian given by

$$\mathbf{H} \triangleq [\mathbf{G} \quad \mathbf{\Gamma}], \quad \mathbf{\Gamma} \triangleq \begin{bmatrix} \mathbf{1}_{N_1} & \dots & \mathbf{0} \\ \vdots & \ddots & \vdots \\ \mathbf{0} & \dots & \mathbf{1}_{N_L} \end{bmatrix} \quad (8)$$

$$\mathbf{G} \triangleq \begin{bmatrix} \frac{[\hat{\mathbf{r}}_r^{(j)}(k) - \mathbf{r}_{s_1}]^T}{\sqrt{\|\hat{\mathbf{r}}_r^{(j)}(k) - \mathbf{r}_{s_1}\|_2^2 + \Delta z_{r,s_1}^2(k)}} \\ \vdots \\ \frac{[\hat{\mathbf{r}}_r^{(j)}(k) - \mathbf{r}_{s_N}]^T}{\sqrt{\|\hat{\mathbf{r}}_r^{(j)}(k) - \mathbf{r}_{s_N}\|_2^2 + \Delta z_{r,s_N}^2(k)}} \end{bmatrix} \quad (9)$$

and $\mathbf{1}_{N_l} \triangleq [1, \dots, 1]^T$. Note that

$$l(n) = \begin{cases} 1, & \text{for } n = 1, \dots, N_1 \\ 2, & \text{for } n = N_1 + 1, \dots, \sum_{l=1}^2 N_l \\ \vdots & \vdots \\ L, & \text{for } n = \sum_{l=1}^{L-1} N_l + 1, \dots, N. \end{cases} \quad (10)$$

After convergence [i.e., $\hat{\mathbf{x}}^{(j+1)}(k) \approx \hat{\mathbf{x}}^{(j)}(k)$] the final estimate is obtained by setting $\hat{\mathbf{x}}(k) \equiv \hat{\mathbf{x}}^{(j+1)}(k)$. In the rest of this article, it is assumed that \mathbf{H} is always full column rank. Observability conditions and their relation to the rank of \mathbf{H} has been studied in [79] and [80]. It is important to note that this article makes the assumption that \mathbf{R}_η is diagonal. In practice, it may not be. In this case, a degradation in the performance is expected. To fully address this issue, the correlation between ϵ_n must be characterized and accounted for in \mathbf{R}_η . Characterizing these correlations is rather involved and is deferred for future work. The sequel assumes that \mathbf{R}_η remains diagonal.

D. Common Clock Bias Parametrization

Note that the clock bias clusters $\{c\delta t_l\}_{l=1}^L$ are “virtual clock biases,” which are introduced to group SOPs whose carrier frequency is more synchronized than others. This would in turn yield more precise measurement models, reducing the estimation error. This section parameterizes $c\delta t_l$ as a function of $c\bar{\delta}t_n$. This parametrization is based on the following theorem.

THEOREM III.1: Consider $N \geq 3$ carrier phase measurements. Assume that the contribution of the relative clock deviation ϵ_n is much larger than the carrier phase measurement noise v_n and that ϵ_n are uncorrelated with identical variances σ^2 . Then, the position error at any time instant $\delta \mathbf{r}_r(k)$ due to relative clock deviations is independent of $c\delta t_l$.

PROOF: See Appendix A.

In plain words, Theorem III.1 is saying that the position error is fully characterized by $\{\epsilon_n\}_{n=1}^N$, assuming it dominates the measurement noise, regardless of the actual values of $\{c\delta t_l\}_{l=1}^L$. The assumption that the contribution of the relative clock deviation ϵ_n is much larger than the carrier phase measurement noise v_n comes from experimental data, where $\|\epsilon\|_2$ was observed to be within 0.2 and 4 m, whereas σ_n was on the order of a few cm. To illustrate that, Fig. 4(a) shows the time history of ϵ_n for the three BTSs shown in Fig. 1 over 24 h, from which it is clearly seen that $\|\epsilon\|_2$ can be in the order of a few meters. Although ϵ_n is stable, Fig. 4(b) shows that the process appears to be initially

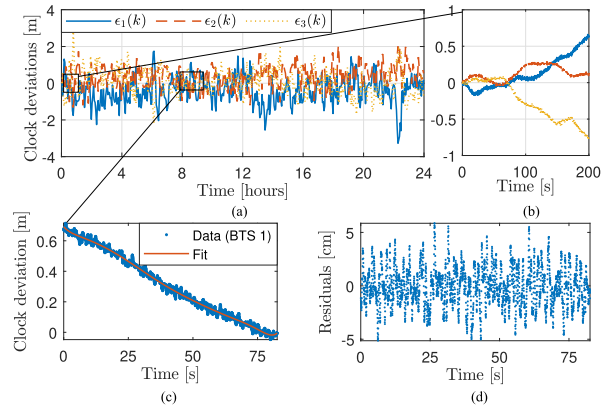


Fig. 4. (a) Time history of ϵ_n for the three BTSs shown in Fig. 1 over 24 h. (b) First 200 s of $\epsilon_n(k)$ showing that the clock deviation process appears to have a diverging short-term behavior. (c) A 75-s portion of ϵ_1 around the eighth hour, as well as a polynomial fit. (d) Residuals between the data and the polynomial fit, whose standard deviation was calculated to be 1.85 cm.

diverging. This apparently diverging short-term behavior is also discussed in Section IV-A. Fig. 4(c) shows a 75-s portion of ϵ_1 around the eighth hour, as well as a polynomial fit. The residuals between the data and the polynomial fit are shown in Fig. 4(d), whose standard deviation was calculated to be 1.85 cm. These residuals contain the effect of $v_1(k)$ as well as $w_{\epsilon_1}(k)$; therefore, σ_n is upper bounded by 1.85 cm, which validates the assumption that the relative clock deviation ϵ_n is much larger than the carrier phase measurement noise v_n .

The reparametrization of $c\bar{\delta}t_n(k)$ in (4) does not assume a specific mapping to $c\delta t(k)$ and $\epsilon_n(k)$ other than being the sum of the two latter terms. Theorem III.1 shows that for a given clustering, the clock bias error term contributing the receiver position error (denoted $\tilde{\epsilon}_n$ in Appendix A) are only a function of 1) $\{c\bar{\delta}t_n\}_{n=1}^N$ and 2) the SOP clock bias clustering [see (36)]. Following the result in (36), the following parametrization is adopted

$$c\delta t_l(k) \equiv \frac{1}{N_l} \sum_{i=1}^{N_l} c\bar{\delta}t_{l_i}(k), \quad \epsilon_n(k) \equiv c\bar{\delta}t_n(k) - c\delta t_{l(n)}(k) \quad (11)$$

where $l_i \triangleq (\sum_{u=1}^{l-1} N_u) + i$, for $i \in 1, \dots, N_l$. The term $c\delta t_l(k)$ is equivalent to $c\delta t(k)$ in (4) for the case of multiple clusters. Note that the UAV can perform an exhaustive search over the different clustering possibilities to minimize its position error while it has access to GPS. The number of possible clusters is given by $N_{\text{clus}} = \sum_{L=1}^{N-2} \binom{N}{L} = \sum_{L=1}^{N-2} \frac{N!}{L!(N-L)!}$. It can be seen that this number becomes impractically large as N increases. A rule-of-thumb that significantly reduces N_{clus} is discussed in Section III-G. Note that it is assumed that cycle slips in the receiver are uncommon. As such, they will be treated as almost constant offsets and will not affect the clustering process.

E. Statistics of the Clock Deviations

It was found that ϵ_n is appropriately modeled to evolve according to the ARMA model given by [25]

$$\begin{aligned} \epsilon_n(k+1) &= \sum_{i=1}^p \phi_i \epsilon_n(k-i+1) \\ &+ \sum_{i=1}^q \psi_i w_{\epsilon_n}(k-i+1) + w_{\epsilon_n}(k) \end{aligned} \quad (12)$$

where p and $\{\phi_i\}_{i=1}^p$ are the order and the coefficients of the autoregressive (AR) part, respectively; q and $\{\psi_i\}_{i=1}^q$ are the order and the coefficients of the moving average (MA) part, respectively; and w_ϵ is a white sequence. Identifying p and q and their corresponding coefficients can be readily obtained with standard system identification techniques [81], and it was found that $p = q = 6$ was usually enough to whiten w_{ϵ_n} [25]. Therefore, ϵ_n will also be a Gaussian sequence. Without loss of generality, it is assumed that $\epsilon_n(i-p) = 0$ for $i = 1, \dots, p$. Subsequently, $\mathbb{E}[\epsilon_n(k)] = 0$. The variance of $\epsilon_n(k)$ is discussed next. The ARMA process in (12) may be represented in state-space according to

$$\xi_n(k+1) = \mathbf{F}_{\xi_n} \xi_n(k) + \mathbf{\Gamma}_{\xi_n} w_{\epsilon_n}(k) \quad (13)$$

$$\epsilon_n(k) = \mathbf{h}_{\epsilon_n}^T \xi_n(k) \quad (14)$$

where ξ_n is the underlying dynamic AR process, \mathbf{F}_{ξ_n} is its state transition matrix, $\mathbf{\Gamma}_{\xi_n}$ is the input matrix, and $\mathbf{h}_{\epsilon_n}^T$ is the output matrix. The eigenvalues of \mathbf{F}_{ξ_n} were computed to be inside the unit circle, implying stability of ξ_n . The covariance of ξ_n , denoted \mathbf{P}_{ξ_n} , evolves according to

$$\mathbf{P}_{\xi_n}(k+1) = \mathbf{F}_{\xi_n} \mathbf{P}_{\xi_n}(k) \mathbf{F}_{\xi_n}^T + \mathbf{Q}_{\xi_n} \quad (15)$$

where $\mathbf{Q}_{\xi_n} \triangleq \sigma_{w_{\epsilon_n}}^2 \mathbf{\Gamma}_{\xi_n} \mathbf{\Gamma}_{\xi_n}^T$ and the variance of the clock deviation ϵ_n at any given time-step is given by

$$\sigma_{\epsilon_n}^2(k) = \mathbf{h}_{\epsilon_n}^T \mathbf{P}_{\xi_n}(k) \mathbf{h}_{\epsilon_n}. \quad (16)$$

Since ξ_n is stable, $\mathbf{P}_{\xi_n}(k)$ will converge to a finite steady-state covariance denoted $\mathbf{P}_{\xi_n,ss}$ given by the solution to the discrete-time matrix Lyapunov equation

$$\mathbf{P}_{\xi_n,ss} = \mathbf{F}_{\xi_n} \mathbf{P}_{\xi_n,ss} \mathbf{F}_{\xi_n}^T + \mathbf{Q}_{\xi_n}. \quad (17)$$

Subsequently, the steady-state variance of the clock deviation is given by

$$\sigma_{\epsilon_n}^2 = \mathbf{h}_{\epsilon_n}^T \mathbf{P}_{\xi_n,ss} \mathbf{h}_{\epsilon_n}. \quad (18)$$

F. Statistics of the Residuals

In this section, the resulting residuals w_ϵ are studied. To this end, the autocorrelation function (acf) and the probability density function (pdf) of the residuals are computed for the three realizations of ϵ_n shown in Fig. 4. Note that half of the data was used for system identification and the other half was used to validate the model. The acf and pdf of the residuals obtained with the second half of the data are plotted in Fig. 5(a)–(c). A Gaussian pdf fit (red) was also plotted. It can be seen that $\{w_{\epsilon_n}\}_{n=1}^3$ are zero-mean white Gaussian sequences, with variances $\{\sigma_{w_{\epsilon_n}}^2\}_{n=1}^3$.

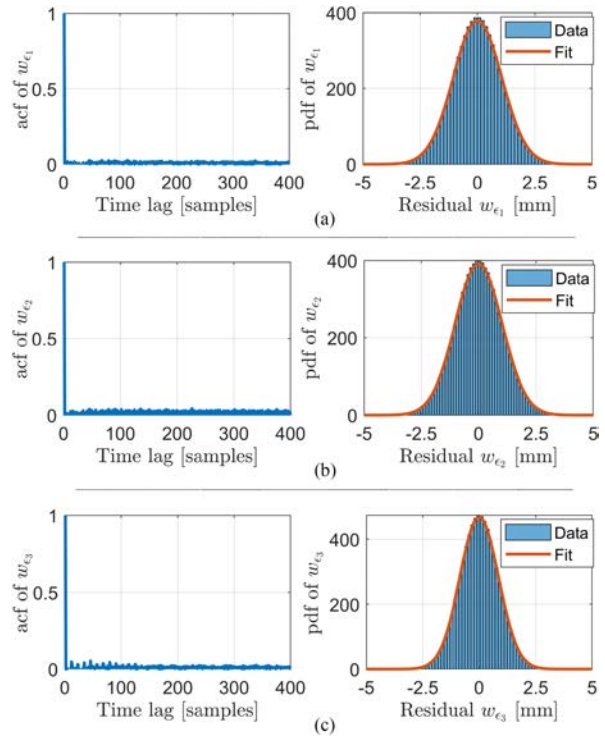


Fig. 5. (a), (b), and (c) show the acfs and pdfs of w_{ϵ_1} , w_{ϵ_2} , and w_{ϵ_3} , respectively. The acfs show that the sequences $\{w_{\epsilon_n}\}_{n=1}^3$ are approximately white and the pdfs show that the sequences are Gaussian.

G. Clustering of the Clock Biases

It was mentioned in Section III-D that an exhaustive search may be performed to cluster the clock biases $c\delta t_n$ in order to minimize the position estimation error. This amounts to finding the matrix $\mathbf{\Gamma}$ that minimizes

$$\begin{aligned} J_p(\mathbf{\Gamma}) &\triangleq \sum_{k=1}^{k_0} \|\delta \mathbf{r}_r(k)\|_2^2 = \\ &\sum_{k=1}^{k_0} \left\| \left[\mathbf{G}^T (\mathbf{I} - \mathbf{\Gamma} (\mathbf{\Gamma}^T \mathbf{\Gamma})^{-1} \mathbf{\Gamma}^T) \mathbf{G} \right]^{-1} \mathbf{G}^T (\mathbf{I} - \mathbf{\Gamma} (\mathbf{\Gamma}^T \mathbf{\Gamma})^{-1} \mathbf{\Gamma}^T) \boldsymbol{\epsilon}(k) \right\|_2^2 \\ &= \sum_{k=1}^{k_0} \left\| (\mathbf{G}^T \boldsymbol{\Psi} \mathbf{G})^{-1} \mathbf{G}^T \boldsymbol{\Psi} \boldsymbol{\epsilon}(k) \right\|_2^2 \end{aligned} \quad (19)$$

where $\mathbf{\Gamma}$ and $\boldsymbol{\Psi}$ are defined in (8) and (33), respectively. This optimization problem is nonconvex and intractable. Instead of optimizing $J_p(\mathbf{\Gamma})$, a tractable rule-of-thumb is provided next. First, consider the modified cost function

$$\begin{aligned} J(\mathbf{\Gamma}) &\triangleq \left\| (\mathbf{G}^T \boldsymbol{\Psi} \mathbf{G})^{-1} \mathbf{G}^T \boldsymbol{\Psi} \boldsymbol{\epsilon}(k_0) \right\|_2^2 \\ &= \left\| (\mathbf{G}^T \boldsymbol{\Psi} \mathbf{G})^{-1} \mathbf{G}^T \boldsymbol{\Psi} \boldsymbol{\epsilon}(k_0) \right\|_2^2 \\ &\leq \left\| (\mathbf{G}_r^T \mathbf{G}_r)^{-1} \mathbf{G}_r^T \right\|_2^2 \left\| \boldsymbol{\Psi} \boldsymbol{\epsilon}(k_0) \right\|_2^2 \end{aligned} \quad (20)$$

where $\mathbf{G}_r \triangleq \boldsymbol{\Psi} \mathbf{G}$. Using the fact that the square of the two-norm of some real matrix \mathbf{A} is the maximum eigenvalue of $\mathbf{A} \mathbf{A}^T$ [82, p. 266 and 341], denoted by $\lambda_{\max}(\mathbf{A} \mathbf{A}^T)$, one can

show that

$$\left\| (\mathbf{G}_\Gamma^T \mathbf{G}_\Gamma)^{-1} \mathbf{G}_\Gamma^T \right\|_2^2 = \lambda_{\max}(\mathbf{P}_{r_r}) \quad (21)$$

where $\mathbf{P}_{r_r} \triangleq (\mathbf{G}_\Gamma^T \mathbf{G}_\Gamma)^{-1}$ is the estimation error covariance associated with the receiver's position. Consequently, the cost $J(\mathbf{\Gamma})$ may be bounded by

$$J(\mathbf{\Gamma}) \leq \lambda_{\max}(\mathbf{P}_{r_r}) \|\Psi \boldsymbol{\epsilon}(k_0)\|_2^2. \quad (22)$$

Next, two theorems are presented that will help derive the rule-of-thumb for clustering the clock biases.

THEOREM III.2 Assume a clock bias clustering with $L < N - 2$ clusters and denote $J_L \triangleq \|\Psi \boldsymbol{\epsilon}(k)\|_2^2$. Then, there exists a clustering with $L + 1$ clusters such that $J_L \geq J_{L+1}$.

PROOF See in Appendix B.

From Theorem III.2, it can be implied that $\|\Psi \boldsymbol{\epsilon}(k)\|_2^2$ is minimized when $L = N - 2$, i.e., the maximum number of clusters is used. This also implies that using more SOP clusters will decrease $\|\Psi \boldsymbol{\epsilon}(k_0)\|_2^2$ in the upper bound expression of $J(\mathbf{\Gamma})$ given in (22).

THEOREM III.3 Consider $N \geq 3$ carrier phase measurements for estimating the receiver's position \mathbf{r}_r and a clustering of L clock states $c\delta t$. Adding a carrier phase measurement from an additional cellular SOP while augmenting the clock state vector $c\delta t$ by its corresponding additional clock state will neither change the position error nor the position error uncertainty.

PROOF: See in Appendix C.

From Theorem III.3, it can be implied that it is required that $N_l \geq 2$ in order for cluster l to contribute in estimating the position state; hence, reducing $\lambda_{\max}(\mathbf{P}_{r_r})$.

Theorems III.2 and III.1 pose a tradeoff on L . On the one hand, Theorem III.2 states that increasing L decreases $\|\Psi \boldsymbol{\epsilon}(k)\|_2^2$. On the other hand, Theorem III.1 states that L must be decreased to decrease $\lambda_{\max}(\mathbf{P}_{r_r})$. Consequently, a good rule of thumb is to have at least one cluster with $N_l \geq 3$ (to ensure observability) and $N_l \geq 2$ for the remaining clusters. Combined with (6), this implies that L should satisfy

$$L \leq L_{\max} \triangleq \frac{N - 3}{2} + 1 \quad (23)$$

which significantly reduces the number of possible clusters in the exhaustive search algorithm, which is summarized in Algorithm 1. The algorithm produces the matrix $\mathbf{\Gamma}$, which is then used to solve the WNLS. It is important to note that the tradeoff on L is similar to the tradeoff between accuracy and precision discussed in [82], to which the reader is referred for more mathematical details. While clustering is performed, the UAV navigates using its known position.

IV. EXPERIMENTAL RESULTS

This section presents results from three experiments conducted in different environments at different times demonstrating submeter-level UAV navigation in

Algorithm 1: Clock bias clustering algorithm.

- 1: **input:** $\{\{z_n(k)\}_{k=1}^{k_0}, \mathbf{r}_{s_n}\}_{n=1}^N, \{\mathbf{r}_r(k)\}_{k=0}^{k_0}$.
 - 2: **output:** $L, \mathbf{\Gamma}, \{c\delta t_l\}_{l=1}^L$.
 - 3: **procedure** Cluster $\{c\delta t_n\}_{n=1}^N$
 - 4: Compute the maximum number of clusters L_{\max} from (23)
 - 5: Perform clustering when GPS is available.
 - 6: **if** GPS available **then**
 - 7: **for** $L = 1$ to L_{\max} **do**
 - 8: Find all possible combinations of L clusters.
 - 9: Evaluate (19) for each combination of clusters.
 - 10: Save the combination of clusters that minimizes (19)
 - 11: Select the clustering that minimizes (19) over all values of L .
 - 12: Form the $N \times L$ matrix $\mathbf{\Gamma}$ according to the clustering: the n th row of $\mathbf{\Gamma}$ is all zeros with a 1 in the l th column, where l is the index of the cluster in which ϵ_n belongs.
-

multipath-free environments using the framework developed in this article. As mentioned in Section II, only the 2-D position of the UAV is estimated as its altitude may be obtained using other sensors (e.g., altimeter). The UAV's position is estimated in the horizontal plane of an East-North-Up (ENU) frame centered at the average of the BTS positions. In the following experiments, the altitude of the UAV was obtained from its on-board navigation system. Alternatively, the UAV's altitude may be obtained from a barometric altimeter. Moreover, the noise equivalent bandwidths of the receivers' PLLs were set to $B_{\text{PLL}} = 3$ Hz in all experiments. The experiment setups and results are discussed next.

A. Experiment 1

In the first experiment, an Autel Robotics X-Star Premium UAV was equipped with an Ettus E312 universal software radio peripheral (USRP), a consumer-grade 800/1900 MHz cellular antenna, and a small consumer-grade GPS antenna to discipline the on-board oscillator. The receiver was tuned to a 882.75 MHz carrier frequency (i.e., $\lambda = 33.96$ cm), which is a cellular CDMA channel allocated for the U.S. cellular provider Verizon Wireless. Samples of the received signals were stored for offline postprocessing. The cellular carrier phase measurements were given at a rate of 37.5 Hz, i.e., $T = 0.0267$ s. The ground-truth reference for the UAV trajectory was taken from its on-board integrated navigation system, which uses GPS, an inertial measurement unit (IMU), and other sensors. The UAV traversed a trajectory of 1.72 km, which was completed in 3 min with a trajectory radius of 270 m. The trajectory radius is defined as the distance between the center of the trajectory and the furthest point on the trajectory.

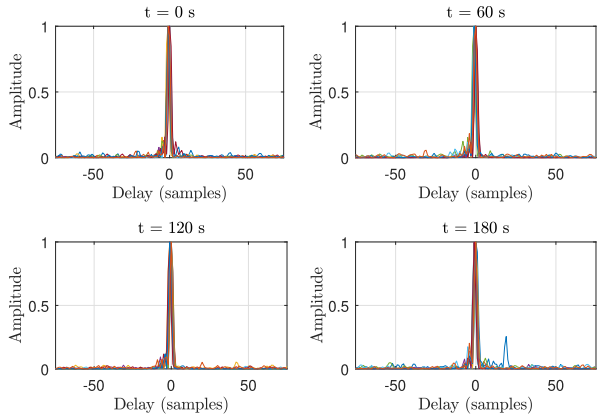


Fig. 6. Channel impulse response measured using the autocorrelation function of the CDMA shortcode for all 9 BTSs over 180 s in the environment near Riverside, California, USA.

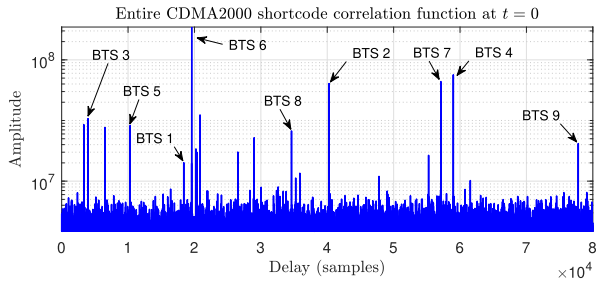


Fig. 7. Entire CDMA2000 shortcode correlation showing multiple peaks pertaining to the different BTSs in the environment.



Fig. 8. Panorama of the environment from the UAV's vantage point for the environment near Riverside, California, USA.

Over the course of the experiment, which took place in an open semiurban environment with multipath-free LOS conditions near Riverside, California, USA, the receiver was listening to 9 CDMA BTSs whose 3-D positions were mapped prior to the experiment according to the framework in [56] and refined using Google Earth. A panorama of the environment from the UAV's vantage point is shown in Fig. 8, and the channel impulse response measured using the autocorrelation function of the CDMA shortcode for all 9 BTSs over 180 s is shown in Fig. 6. The curves in Fig. 6 demonstrate a dominant LOS component and nearly multipath-free conditions. Similar channels were observed for the second and third experiments. The entire correlation of the CDMA2000 shortcode is shown in Fig. 7. A plot of

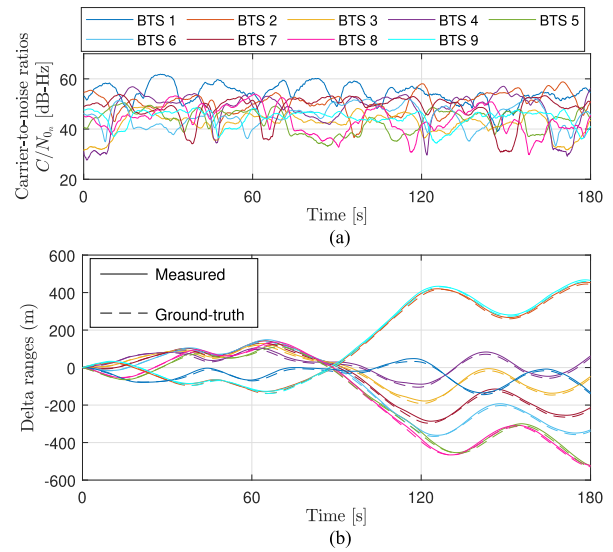


Fig. 9. (a) Carrier-to-noise ratios $\{C/N_{0n}\}_{n=1}^9$ of all the cellular BTSs measured by the UAV in the CD-cellular experiment. (b) Measured and calculated delta ranges to all the cellular BTSs from the UAV in the CD-cellular experiment. Similarly, the base's measured delta ranges closely matched the calculated delta ranges.

the carrier-to-noise ratios of all the BTSs measured by the UAV and the time history of the delta ranges (deviation from the initial range) are given in Fig. 9(a) and (b), respectively.

The UAV had access to GPS for 10 s, then GPS was cut off. During the time where GPS was available, the cellular signals were used to cluster the cellular SOPs, as described in Section III-G. The BTS clock biases obtained from ground-truth are shown in Fig. 10(a) for all nine BTSs. While Fig. 10(a) shows $\{c\delta t_n(k)\}_{n=1}^9$ for the entire trajectory, only the first 10 s were used for clustering. The optimal clustering was found to be $C_1 = \{\text{BTS 1, BTS 5, BTS 7, BTS 8}\}$, $C_2 = \{\text{BTS 2, BTS 3, BTS 6}\}$, and $C_3 = \{\text{BTS 4, BTS 9}\}$. The resulting clock deviations $\{\epsilon_n\}_{n=1}^9$ and the cluster clock biases $\{c\delta t_l\}_{l=1}^3$ are shown in Fig. 10(b) and (c), respectively. Note that $\{\epsilon_n\}_{n=1}^9$ appear to be diverging, similarly to the behavior in Fig. 4(b). However, it is found next that these processes are stable.

Then, the state-space models of $\{\epsilon_n\}_{n=1}^9$ were identified according to Section III-E for $p = q = 6$ using MATLAB's System Identification Toolbox. Appendix D shows the ARMA coefficients as well as the resulting $\{\sigma_{w_{\epsilon_n}}\}_{n=1}^9$. Fig. 11 shows the residuals between $\{\epsilon_n\}_{n=1}^9$ and the identified models, which were found to be white sequences. The steady-state values of $\{\sigma_{\epsilon_n}\}_{n=1}^9$ were calculated from (18) and used in the WNLS.

Next, the time evolution of $\{\sigma_{\epsilon_n}^2\}_{n=1}^9$ and their steady-state values were computed according to Section III-E. Fig. 12 shows the time evolution of $\{\sigma_{\epsilon_n}\}_{n=1}^9$. The time axis was extended longer than the experiment duration to show the convergence of $\{\sigma_{\epsilon_n}\}_{n=1}^9$, indicating that $\{\epsilon_n\}_{n=1}^9$ are stable processes.

Subsequently, the position of the UAV and the clusters' clock biases were estimated according to Section III-C. The

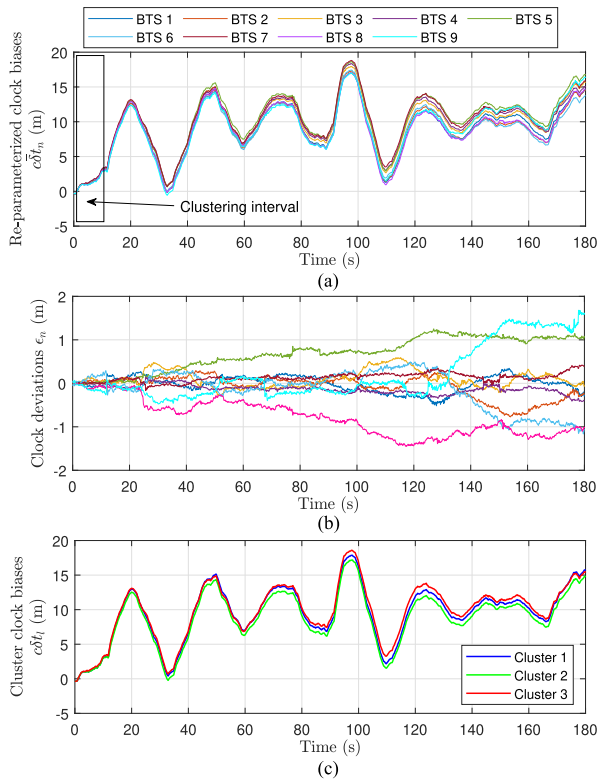


Fig. 10. (a) BTS Clock biases in Experiment 1 obtained from ground-truth. (b) Deviations of the BTS clock biases after clustering. Note that the legend of (b) is the same as (a). (c) BTS clusters' clock biases. Clustering was performed in the first 10 seconds while GPS was available.

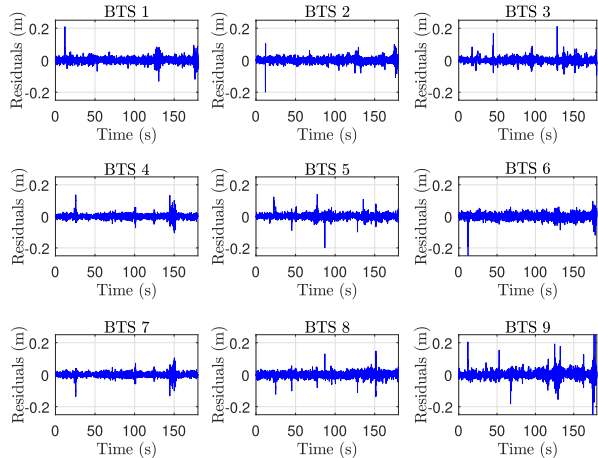


Fig. 11. Residuals of the clock deviation ARMA models for all the nine BTSs in Experiment 1 obtained using MATLAB's System Identification Toolbox for $p = q = 6$. A correlation analysis shows that the residuals are white.

horizontal position RMSE was calculated to be 36.61 cm. The carrier phase measurements were used to estimate the navigating UAV's trajectory via the framework developed in Section III. The experimental setup, the cellular BTS layout, and the true trajectory (from the UAV's on-board integrated navigation system) and estimated trajectory (from the proposed framework) of the navigating UAV are shown in Fig. 13, the x - and y - errors over the entire trajectory are

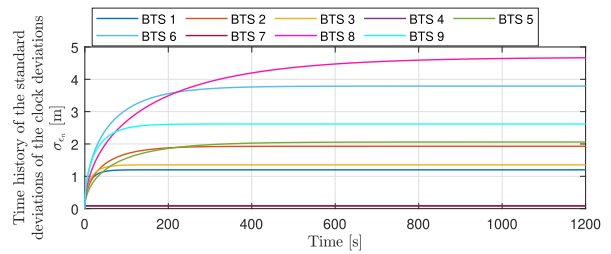


Fig. 12. Time evolution of $\{\sigma_{\epsilon_n}\}_{n=1}^9$ calculated according to Section III-E. The time axis was extended longer than the experiment duration to show the convergence of $\{\sigma_{\epsilon_n}\}_{n=1}^9$ are stable processes.

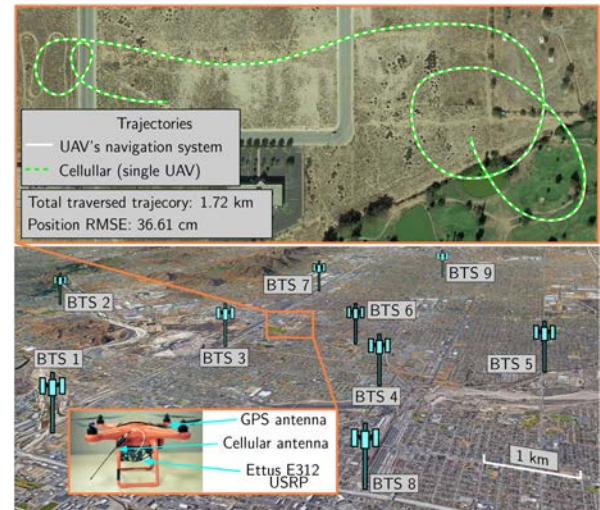


Fig. 13. Experiment 1 setup, BTS layout, and navigation solution demonstrating a single UAV navigating with precise cellular carrier phase measurements. The true and estimated trajectories are shown in solid and dashed lines, respectively. Map data: Google Earth.

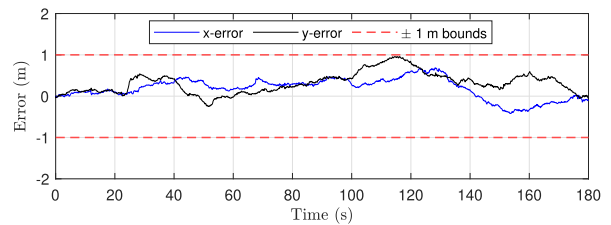


Fig. 14. Experiment 1 x - and y -errors over the entire trajectory as well as the ± 1 m bounds showing that the position errors remain below 1 meter throughout the experiment.

shown in Fig. 14, and the estimated cluster clock biases are shown in Fig. 15.

Next, the frequency of clock bias clustering is considered. That is, it is assumed that the UAV regains knowledge of its position for a short period of time throughout the experiment either through the CD-cellular framework (e.g., flying in the vicinity of a base) or via GPS. During these short periods, the UAV updates the clock bias clusters. To this end, the frequency at which the UAV performs clustering was varied from 1 to 2, and then to 4 times during the experiment. The clustering events were uniformly spaced in time. Every time the UAV regains of its position, the

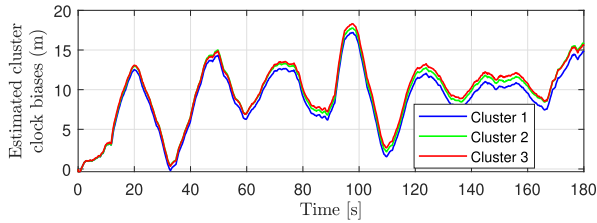


Fig. 15. Estimated cluster clock biases for the first experiment. The estimated biases match closely the cluster biases shown in Fig. 10(c).

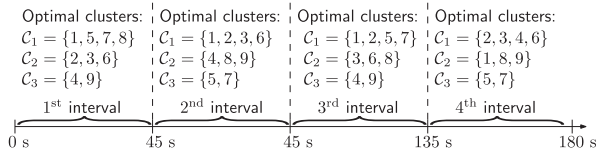


Fig. 16. Optimal BTS clusters for each interval in Experiment 1.

latter is made available for 10 s to perform clustering and is cut off again. The position RMSEs were found to be 36.61, 45.11, and 18.1 cm for clustering frequencies of 1, 2, and 4, respectively. The optimal clusters for each interval of the trajectory are shown in Fig. 16. Note that new initial clock bias estimates are produced every time clustering is performed.

B. Experiment 2

In the second experiment, a DJI Matrice 600 was equipped with the same hardware described in Section IV-A and the on-board USRP was tuned to the same carrier frequency. The cellular carrier phase measurements were also given at a rate of 37.5 Hz, i.e., $T = 0.0267$ s. The ground-truth reference for the UAV trajectory was taken from its on-board navigation system, which also uses GPS, an IMU, and other sensors. The experimental setup and SOP BTS layout for the second experiment are shown in Fig. 17. The ground-truth reference for the UAV trajectory was taken from its on-board integrated navigation system, which also uses GPS, IMU, and other sensors. The UAV traversed a trajectory of 3.07 km completed in 325 s with a trajectory radius of 320 m. The receiver was listening to the seven CDMA BTSs shown in Fig. 17. The UAV remained in the same BTS sectors throughout the experiments. A plot of the carrier-to-noise ratios of all the BTSs and the time history of the delta ranges are given in Fig. 19(a) and (b), respectively. The same steps as in Experiment 1 were taken to cluster the BTS clock biases and characterize the clock deviation statistics. The optimal clustering for a one-time clustering was found to be $C_1 = \{\text{BTS 1}, \text{BTS 2}, \text{BTS 3}, \text{BTS 4}, \text{BTS 6}\}$ and $C_2 = \{\text{BTS 5}, \text{BTS 7}\}$. The position RMSE was calculated to be 88.58 cm. The navigation results are shown in Fig. 17 and the x - and y - errors are shown in Fig. 18.

A similar study as in Experiment 1 is performed to characterize the RMSE under varying clustering frequencies. The same approach was taken as in the previous experiment. The position RMSEs were found to be 88.58, 84.17, and 83.07 cm for clustering frequencies of 1, 2, and 4, respectively.

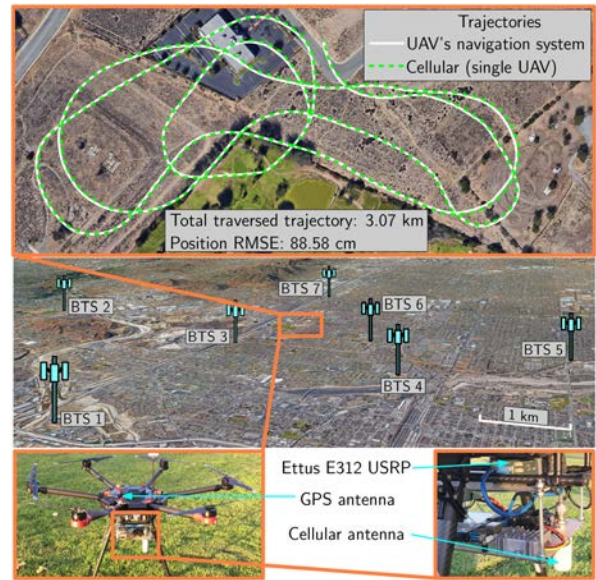


Fig. 17. Experiment 2 setup, BTS layout, and navigation solution demonstrating a single UAV navigating with precise cellular carrier phase measurements. The true and estimated trajectories are shown in solid and dashed lines, respectively. Map data: Google Earth.

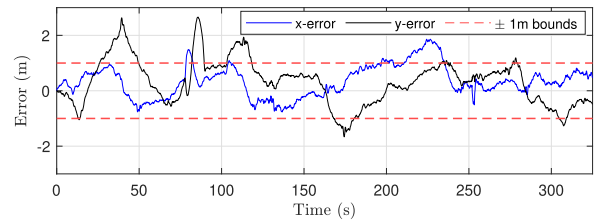


Fig. 18. Experiment 2 x - and y -errors over the entire trajectory as well as the ± 1 m bounds showing that the position errors remain below 1 meter most of the time.

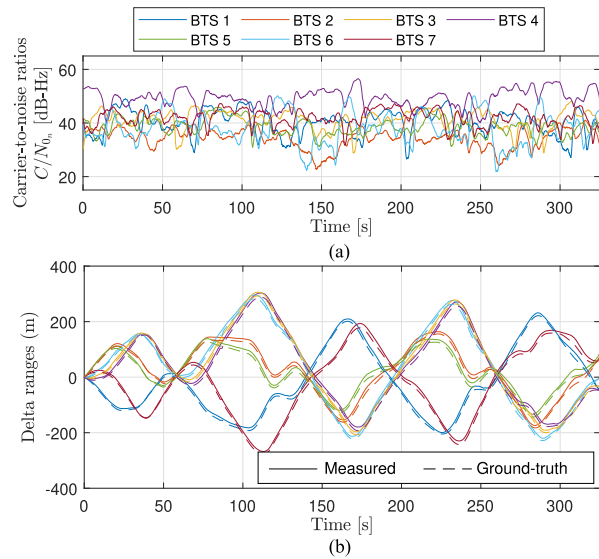


Fig. 19. (a) Carrier-to-noise ratios $\{C/N_{0n}\}_{n=1}^7$ of all the cellular BTSs measured by the single UAV in Experiment 2. (b) Measured and calculated delta ranges to all the cellular BTSs from the single UAV.

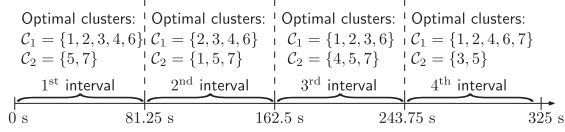


Fig. 20. Optimal BTS clusters for each interval in Experiment 2.



Fig. 21. Panorama of the environment from the UAV's vantage point for the environment in Aliso Viejo, California, USA.

The optimal clusters for each interval of the trajectory are shown in Fig. 20.

C. Experiment 3

In the third experiment, the Matrice UAV was equipped with 1) a four-channel National Instrument (NI) USRP-2955 to sample LTE signals at four different carrier frequencies; 2) four consumer-grade 800/1900 MHz cellular antennas; 3) a small consumer-grade GPS antenna to discipline the on-board oscillator; and 4) a dual antenna, multi-frequency Septentrio AsteRx-i V GNSS-inertial navigation system (INS) with RTK capabilities to provide ground-truth of the UAV's position and attitude. The four receiver channels were tuned to 1955 MHz ($\lambda = 15.33$ cm), 2145 MHz ($\lambda = 13.98$ cm), 2125 MHz ($\lambda = 14.11$ cm), and 739 MHz ($\lambda = 40.57$ cm), which are all LTE frequencies and allocated to the U.S. cellular operators AT&T, T-Mobile, and Verizon. Over the course of the experiment, which took place in an open semiurban environment with multipath-free LOS conditions near Aliso Viejo, California, USA, the receivers were listening to 11 LTE BTSs, also known as eNBs, whose 3-D positions were also mapped prior to the experiment according to the framework in [56] and refined using Google Earth. A panorama of the environment from the UAV's vantage point is shown in Fig. 21.

In this experiment, the cellular carrier phase measurements were given at a rate of 1 Hz, i.e., $T = 1$ s. The UAV traversed a trajectory of 609 m completed in 175 s with a trajectory radius of 68 m and remained in the same eNB sectors throughout the experiment. A plot of the carrier-to-noise ratios of all the eNBs and the time history of the delta ranges are given in Fig. 24(a) and (b), respectively. The same steps as in Experiment 1 were taken to cluster the eNB clock biases and characterize the clock deviation statistics. The optimal clustering for a one-time clustering was found to be $\mathcal{C}_1 = \{\text{eNB 2, eNB 8, eNB 9, eNB 10, eNB 11}\}$ and

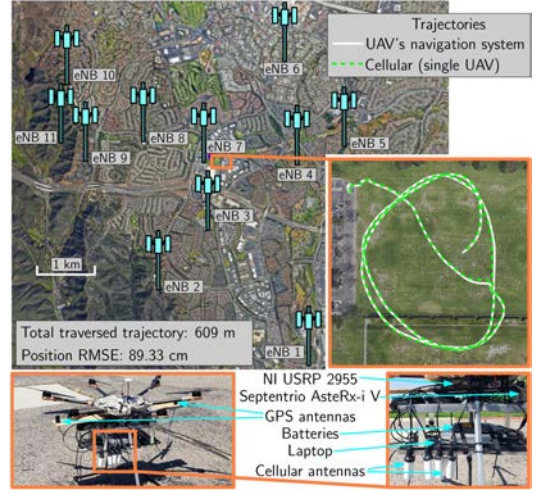


Fig. 22. Experiment 3 setup, eNB layout, and navigation solution demonstrating a single UAV navigating with precise cellular carrier phase measurements. The true and estimated trajectories are shown in solid and dashed lines, respectively. Map data: Google Earth.

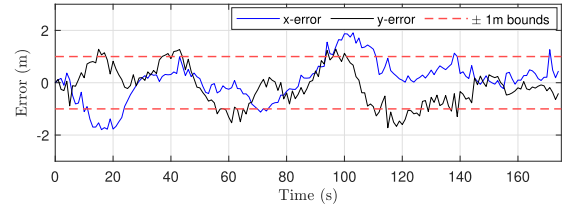


Fig. 23. Experiment 3 x - and y -errors over the entire trajectory as well as the ± 1 m bounds showing that the position errors remain below 1 meter most of the time.

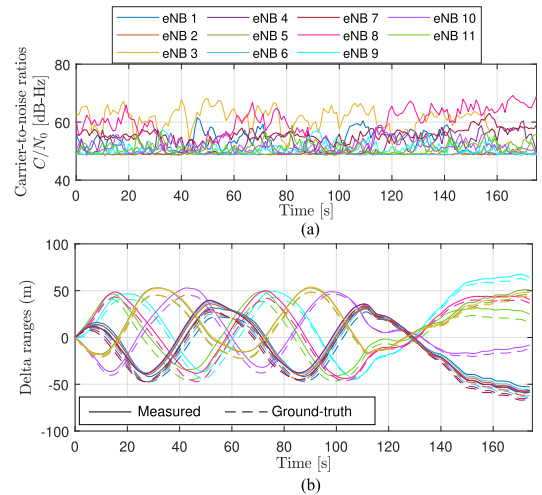


Fig. 24. Measured and calculated delta ranges to all the cellular eNBs from the single UAV in Experiment 3.

$\mathcal{C}_2 = \{\text{eNB 1, eNB 3, eNB 4, eNB 5, eNB 6, eNB 7}\}$. The position RMSE was calculated to be 89.33 cm. The navigation results are shown in Fig. 22 and the x - and y -errors are shown in Fig. 23.

A similar study as in Experiments 1 and 2 is performed to characterize the RMSE under varying clustering frequencies. The same approach was taken as in the previous experiments. The position RMSEs were found to be 89.33,

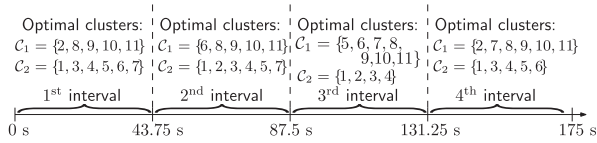


Fig. 25. Optimal eNB clusters for each interval in Experiment 3.

TABLE I
Lowest Position RMSEs for the Three Experiments

	Experiment 1	Experiment 2	Experiment 3
Duration	180 s	325 s	175 s
Distance traveled	1.72 km	3.07 km	0.61 km
Trajectory radius	270 m	320 m	68 m
Position RMSE	18.1 cm	83.07 cm	80.96 cm

TABLE II
Position RMSEs of the Three Experiments for Different Clustering Frequencies

	Clustering frequency		
	1	2	4
Experiment 1	36.61 cm	45.11 cm	18.1 cm
Experiment 2	88.58 cm	84.17 cm	83.07 cm
Experiment 3	89.33 cm	81.07 cm	80.96 cm

TABLE III
Comparison of Position RMSEs for the Exploited Levels of Synchronization

Exploited level of synchronization	Experiment 1	Experiment 2	Experiment 3
Loose	36.6 cm	88.58 cm	89.53 cm
Asynchronous	2.94 m	5.99 m	1.96 m

81.07, and 80.96 cm for clustering frequencies of 1, 2, and 4, respectively. The optimal clusters for each interval of the trajectory are shown in Fig. 25.

The lowest achieved position RMSE for each experiment are tabulated in Table I and the RMSEs for different clustering frequencies are summarized in Table II, which shows that in general, updating the clustering yields better performance than fixing the clusters once at the beginning. The increase in RMSE in Experiment 1 between clustering frequencies of 1 and 2 can be attributed to the diverging short-term behavior of ϵ_n , as discussed above.

REMARK The proposed method assumes a certain level of synchronization between BTSs, referred to as loose synchronization. If this synchronization is completely absent or unexploited using the proposed framework, the method in [79], which addresses asynchronous networks, could be used instead. However, this will come at the cost of larger position errors. For example, the position RMSE of experiment 1 will increase from 36.6 cm to 2.94 m, the position RMSE of experiment 2 will increase from 88.58 cm to 5.99 m [79], and the position RMSE of experiment 3 will increase from 89.53 cm to 1.96 m. These results are summarized in Table III. As such, in the case of the three experiments presented herein, submeter-level position RMSE is achieved by exploiting loose network synchronization using the proposed method in a multipath-free environment with LOS conditions. The RMSEs are calculated relative to a GPS-IMU solution in the case of Experiments 1 and 2,

and relative to an GNSS-IMU RTK system in the case of Experiment 3.

D. Discussion

The following are key takeaways and remarks from the experimental results presented above. First, it is important to note that the RMSEs for the first two experiments were calculated with respect to the trajectory returned by the UAVs' on-board navigation system. Although these systems use multiple sensors for navigation, they are not equipped with high precision GPS receivers, e.g., RTK systems. Therefore, some errors are expected in what is considered to be "true" trajectories taken from the on-board sensors. The hovering horizontal precision of the UAVs are reported to be 2 m for the X-Star Premium by Autel Robotics and 1.5 m for the Matrice 600 by DJI. In contrast, the ground-truth system for the third non-differential single-UAV experimental results uses RTK and is rated at 0.6 cm horizontal precision by Septentrio. Moreover, some errors may be due to uncertainties in the BTS positions, which were obtained from Google Earth imagery. While the accuracy of Google Earth is not officially known, studies show that it is below 20 cm in the areas of interest [83].

Second, the reported RMSEs are for optimal clustering. In the 10 s during which GPS was available, a search was performed to optimally cluster the clock biases using the rule-of-thumb discussed in Section III-G. The search took less than 3 s in each case. The RMSEs without clustering (only one bias is estimated) are 48 cm, 97 cm, and 1.78 m for the first, second, and third single-UAV experiments, respectively. As such, optimal clustering following the analysis proposed in Section III resulted in approximately 24%, 9%, 48% reductions in the position RMSEs, respectively, over not clustering at all.

Third, the experiments showed that reliable navigation with cellular signals is possible when the proper models are used in an open semiurban environment. Some of the experiments went over 5 min, indicating that the UAV could rely *exclusively* on cellular carrier phase measurements for sustained meter-level accurate navigation. Note that the proposed frameworks does not account for unmodeled errors such as multipath or signal blockage. Such errors could be partially mitigated at the receiver level [37]. It is expected for the performance to degrade in the presence of such errors.

Fourth, throughout the experiments, the UAV remained within the same BTS or eNB sectors. BTSs and eNBs typically transmit in three different sectors, each of which covering 120°. When crossing between sectors, the receiver would need to perform a "handover," which involves acquiring and tracking the signal from the new sector [44]. If the BTS sectors are not completely synchronized, the handover may introduce meter-level errors to the BTSs' clock bias model. One way to reduce the effect of the errors introduced by crossing BTS sectors is to use the approach proposed in [24].

Fifth, it was assumed that the UAVs had short access to GPS to perform clustering and initialize proposed framework. Alternatively, if a base receiver is continuously or intermittently present throughout the navigation period, the UAV could leverage the cellular-based differential framework proposed in [51] to perform clustering periodically. This would completely eliminate the dependency on GPS. Moreover, it was shown in [57] that under real GPS jamming conditions, cellular BTSs maintain the same level of synchronization for at least 90 min, and that a cellular SOP receiver can navigate for 5 km in the presence of jamming. This implies that the navigation performance of the proposed framework will not suffer under GPS jamming for a significant period of time.

Sixth, Fig. 12 shows that the clock deviations are stable processes with bounded standard deviations. However, Table II shows that, in general, keeping the same clustering performs worse than updating the clustering when GPS is available. This is due the fact that some of the ϵ_n processes, while stable, reach stationarity at a much slower rate than the rate at which positioning is performed. Therefore, optimal clusters may change in the short-term. In the long-term, if clustering is performed only once, the steady-state values of σ_{ϵ_n} will determine the accuracy of the position solution. According to Fig. 12, $\sigma_{\epsilon_n} < 5$ m, which is equivalent to GPS pseudorange precision. It is also worth mentioning that the ubiquity of cellular SOPs offers a low horizontal dilution of precision (HDOP). In fact, the HDOP remained below unity in all experiments. The low HDOP further reduces the effect of a large σ_{ϵ_n} .

Seventh, the UAV-mounted receiver's clock bias is accounted for as part of the common clock bias terms. As such, the magnitude of the receiver's clock bias should not affect the position estimate. It has been proven in [24] [c.f. (30)] that the position error is independent of common errors, which is the receiver's clock bias in this case. This implies that the quality of the receiver's clock should not affect the navigation performance, as long as the receiver can maintain track of the signals. As an example, the USRPs used in Experiments 1 and 2 are equipped with GPS-disciplined TCXOs, whereas the one used in Experiment 3 was equipped with a GPS-disciplined OCXO; yet, the navigation performances were comparable.

Eighth, in order to assess the effect of altimeter errors on the 2-D navigation solution, a zero-mean, Gaussian measurement noise error was simulated in $\Delta z_{r,s_n}$ with a 100 m² variance. The 2-D position RMSEs for experiments 1, 2, and 3 in the presence of altimeter errors were 38.3 cm (increase of 1.7 cm), 1.03 m (increase of 14.4 cm), and 94.6 cm (increase of 4.3 cm), respectively. The degradation in the 2-D navigation solution is up to two orders of magnitudes less than the altimeter errors.

Ninth, the reclustering idea is related to intermittent self-calibration of clocks using ground-based SOPs [84]. The main difference, however, lies in the fact the proposed method keeps estimating clock biases after reclustering, albeit a subset of the clock biases. The subset of clock biases is selected via the clustering algorithm. This ensures a robust navigation solution against unexpected time varying

behaviors of clock biases while minimizing the number of estimated parameters to reduce the DOP. Moreover, this article assumed periodic reclustering; however, reclustering could be performed whenever the UAV regains access to GPS or following some metric defined by the desired application.

V. CONCLUSION

This article presented a framework for UAV navigation with cellular carrier phase measurements where submeter accuracy is achievable under multipath-free LOS conditions and the UAV not crossing BTS sectors. The proposed framework leverages the relative stability of cellular BTSs clocks, referred to as loose network synchronization. This stability also allows to parameterize the SOP clock biases by a common term plus some small deviations from the common term. The clock deviations were subsequently modeled as a stochastic sequence and the model is validated through extensive experimental data. Analysis of these deviations revealed that they can be clustered to minimize the resulting position error. Next, a rule-of-thumb for clustering the clock deviations was established to significantly reduce the complexity of the clustering step. To demonstrate the efficacy of the developed framework, three UAV flight experiments in Southern California, USA, were presented. The three experiments took place in open, semiurban environments with nearly multipath-free LOS conditions, in which the UAV traveled 1.72, 3.07, and 0.61 km, achieving submeter horizontal position RMSEs of 36.61, 88.58, and 89.33 cm, respectively, relative to the UAV's on-board navigation solution.

APPENDIX A PROOF OF THEOREM III.1

This appendix provides the proof of Theorem III.1 stating that the position error at any time instant $\delta r_r(k)$ due to relative clock deviations is independent of $c\delta t_l$.

PROOF Denote the measurement noise covariance of $\eta \triangleq [\eta_1 \dots \eta_n]^T$ as \mathbf{R}_η . It is assumed that the WNLS had converged very closely to the true state in the absence of clock deviations. The clock deviations are then suddenly introduced into the measurements, which will induce an incremental change in the receiver state estimate given by

$$\begin{aligned} \delta \mathbf{x}(k) &= -(\mathbf{H}^T \mathbf{R}_\eta^{-1} \mathbf{H})^{-1} \mathbf{H}^T \mathbf{R}_\eta^{-1} \boldsymbol{\epsilon}(k) \\ &= -(\bar{\mathbf{H}}^T \bar{\mathbf{H}})^{-1} \bar{\mathbf{H}}^T \bar{\boldsymbol{\epsilon}}(k) \end{aligned} \quad (24)$$

where

$$\bar{\mathbf{H}} \triangleq \mathbf{R}_\eta^{-\frac{1}{2}} \mathbf{H}, \quad \bar{\boldsymbol{\epsilon}}(k) \triangleq \mathbf{R}_\eta^{-\frac{1}{2}} \boldsymbol{\epsilon}(k) \quad (25)$$

and $\boldsymbol{\epsilon} \triangleq [\epsilon_1, \dots, \epsilon_N]^T$. The matrix product $\bar{\mathbf{H}}^T \bar{\boldsymbol{\epsilon}}(k)$ can be further expressed as

$$\bar{\mathbf{H}}^T \bar{\boldsymbol{\epsilon}}(k) = \begin{bmatrix} \bar{\mathbf{G}}^T \\ \bar{\mathbf{\Gamma}}^T \end{bmatrix} \bar{\boldsymbol{\epsilon}}(k) = \begin{bmatrix} \bar{\mathbf{G}}^T \bar{\boldsymbol{\epsilon}}(k) \\ \bar{\mathbf{\Gamma}}^T \bar{\boldsymbol{\epsilon}}(k) \end{bmatrix} \quad (26)$$

where

$$\bar{\mathbf{G}} \triangleq \mathbf{R}_\eta^{-\frac{1}{2}} \mathbf{G}, \quad \bar{\mathbf{\Gamma}} \triangleq \mathbf{R}_\eta^{-\frac{1}{2}} \mathbf{\Gamma}. \quad (27)$$

Next, $(\bar{\mathbf{H}}^T \bar{\mathbf{H}})^{-1}$ is expressed as

$$(\bar{\mathbf{H}}^T \bar{\mathbf{H}})^{-1} = \left[\begin{array}{cc} \bar{\mathbf{G}}^T \bar{\mathbf{G}} & \bar{\mathbf{G}}^T \bar{\mathbf{\Gamma}} \\ \bar{\mathbf{\Gamma}}^T \bar{\mathbf{G}} & \bar{\mathbf{\Gamma}}^T \bar{\mathbf{\Gamma}} \end{array} \right]^{-1} \triangleq \left[\begin{array}{cc} \mathbf{A} & \mathbf{B} \\ \mathbf{B}^T & \mathbf{D} \end{array} \right] \quad (28)$$

where \mathbf{A} is a 2×2 symmetric matrix, \mathbf{B} is a $2 \times L$ matrix, and \mathbf{D} is an $L \times L$ symmetric matrix. The estimation error becomes

$$\delta \mathbf{x}(k) = \begin{bmatrix} \delta r_r(k) \\ \delta(c\delta t(k)) \end{bmatrix} = - \left[\begin{array}{c} (\mathbf{A}\bar{\mathbf{G}}^T + \mathbf{B}\bar{\mathbf{\Gamma}}^T) \\ (\mathbf{B}^T\bar{\mathbf{G}}^T + \mathbf{D}\bar{\mathbf{\Gamma}}^T) \end{array} \right] \bar{\boldsymbol{\epsilon}}(k). \quad (29)$$

Using the matrix block inversion lemma, the following may be obtained:

$$\begin{aligned} \mathbf{A} &= (\bar{\mathbf{G}}^T \bar{\boldsymbol{\Psi}} \bar{\mathbf{G}})^{-1} \\ \mathbf{B} &= -(\bar{\mathbf{G}}^T \bar{\boldsymbol{\Psi}} \bar{\mathbf{G}})^{-1} \bar{\mathbf{G}}^T \bar{\mathbf{\Gamma}} (\bar{\mathbf{\Gamma}}^T \bar{\mathbf{\Gamma}})^{-1} \\ \mathbf{D} &= (\bar{\mathbf{\Gamma}}^T \bar{\mathbf{\Gamma}})^{-1} \left[\mathbf{I} + \bar{\mathbf{\Gamma}}^T \bar{\mathbf{G}} (\bar{\mathbf{G}}^T \bar{\boldsymbol{\Psi}} \bar{\mathbf{G}})^{-1} \bar{\mathbf{G}}^T \bar{\mathbf{\Gamma}} (\bar{\mathbf{\Gamma}}^T \bar{\mathbf{\Gamma}})^{-1} \right] \end{aligned} \quad (30)$$

where $\bar{\boldsymbol{\Psi}} \triangleq \mathbf{I} - \bar{\mathbf{\Gamma}} (\bar{\mathbf{\Gamma}}^T \bar{\mathbf{\Gamma}})^{-1} \bar{\mathbf{\Gamma}}^T$. This yields the position error given by

$$\delta r_r(k) = -(\bar{\mathbf{G}}^T \bar{\boldsymbol{\Psi}} \bar{\mathbf{G}})^{-1} \bar{\mathbf{G}}^T \bar{\boldsymbol{\Psi}} \bar{\boldsymbol{\epsilon}}(k). \quad (31)$$

When $\mathbf{R}_\eta = \sigma^2 \mathbf{I}$, the above simplifies to

$$\delta r_r(k) = -(\mathbf{G}^T \boldsymbol{\Psi} \mathbf{G})^{-1} \mathbf{G}^T \boldsymbol{\Psi} \boldsymbol{\epsilon}(k) \quad (32)$$

$$\boldsymbol{\epsilon}(k) \triangleq [\epsilon_1(k), \dots, \epsilon_N(k)]^T, \quad \boldsymbol{\Psi} \triangleq \mathbf{I} - \boldsymbol{\Gamma} (\boldsymbol{\Gamma}^T \boldsymbol{\Gamma})^{-1} \boldsymbol{\Gamma}^T. \quad (33)$$

Note that $\boldsymbol{\Psi}$ is the annihilator matrix of $\boldsymbol{\Gamma}$ and satisfies $\boldsymbol{\Psi} \boldsymbol{\Psi} = \boldsymbol{\Psi}$. It can be readily shown that

$$\boldsymbol{\Psi} = \text{diag} \left[\mathbf{I}_{N_1} - \frac{1}{N_1} \mathbf{1}_{N_1} \mathbf{1}_{N_1}^T, \dots, \mathbf{I}_{N_L} - \frac{1}{N_L} \mathbf{1}_{N_L} \mathbf{1}_{N_L}^T \right]. \quad (34)$$

Consequently, (32) implies that the effect on the position error δr_r comes from the vector

$$\tilde{\boldsymbol{\epsilon}}(k) \triangleq \boldsymbol{\Psi} \boldsymbol{\epsilon}(k) = - \begin{bmatrix} \epsilon_1(k) - \mu_1(k) \mathbf{1}_{N_1} \\ \vdots \\ \epsilon_L(k) - \mu_L(k) \mathbf{1}_{N_L} \end{bmatrix} \quad (35)$$

where $\boldsymbol{\epsilon}(k) = [\boldsymbol{\epsilon}_1^T(k), \dots, \boldsymbol{\epsilon}_L^T(k)]^T$, $\boldsymbol{\epsilon}_l(k) = [\epsilon_{l_1}, \dots, \epsilon_{l_{N_l}}]^T$, and $\mu_l(k) \triangleq \frac{1}{N_l} \sum_{i=1}^{N_l} \epsilon_{l_i}(k)$. Noting that $\epsilon_n(k) = c\delta t_{l(n)}(k) - c\bar{\delta}t_n(k)$, the following holds:

$$\begin{aligned} \tilde{\epsilon}_n(k) &= \frac{1}{N_l} \sum_{i=1}^{N_l} [c\delta t_{l(i)}(k) - c\bar{\delta}t_{l_i}(k)] - [c\delta t_{l(n)}(k) - c\bar{\delta}t_n(k)] \\ &= c\bar{\delta}t_n(k) - \frac{1}{N_l} \sum_{i=1}^{N_l} c\bar{\delta}t_{l_i}(k) \end{aligned} \quad (36)$$

which is independent of $c\delta t_l(k)$. \square

APPENDIX B

PROOF OF THEOREM III.2

This appendix provides the proof of Theorem III.2, which states that given a clock bias clustering with $L < N - 2$ clusters and $J_L \triangleq \|\boldsymbol{\Psi} \boldsymbol{\epsilon}(k)\|_2^2$; then, there exists a clustering with $L + 1$ clusters such that $J_L \geq J_{L+1}$.

PROOF: First, note that J_L may be expressed as

$$\begin{aligned} J_L &= \|\boldsymbol{\Psi} \boldsymbol{\epsilon}(k)\|_2^2 = \left\| \begin{bmatrix} \boldsymbol{\epsilon}_1(k) - \mu_1(k) \mathbf{1}_{N_1} \\ \vdots \\ \boldsymbol{\epsilon}_L(k) - \mu_L(k) \mathbf{1}_{N_L} \end{bmatrix} \right\|_2^2 \\ &= \sum_{l=1}^L \|\boldsymbol{\epsilon}_l - \mu_l(k) \mathbf{1}_{N_l}\|_2^2 = \sum_{l=1}^L \sum_{j=1}^{N_l} [\epsilon_{l_j}(k) - \mu_l(k)]^2 \\ &= \sum_{l=1}^{L-1} \sum_{j=1}^{N_l} [\epsilon_{l_j}(k) - \mu_l(k)]^2 + \sum_{j=1}^{N_L} [\epsilon_{L_j}(k) - \mu_L(k)]^2 \\ &= a + \sum_{j=1}^{N_L} (\epsilon_{L_j}(k) - \mu_L(k))^2 \end{aligned} \quad (37)$$

where $a \triangleq \sum_{l=1}^{L-1} \sum_{j=1}^{N_l} [\epsilon_{l_j}(k) - \mu_l(k)]^2$. In what follows, the time argument k will be dropped for simplicity of notation. Now, add an additional cluster by partitioning $\boldsymbol{\epsilon}_L$ according to $\boldsymbol{\epsilon}_L = [\boldsymbol{\epsilon}'_L, \boldsymbol{\epsilon}_{L+1}]^T$ and define

$$J_{L+1} = a + \sum_{j=1}^{N_L-1} (\epsilon_{L_j} - \mu'_L)^2 + (\epsilon_{L+1} - \mu_{L+1})^2 \quad (38)$$

where $\mu'_L \triangleq \frac{1}{N_L-1} \sum_{j=1}^{N_L-1} \epsilon_{L_j}$ and $\mu_{L+1} = \epsilon_{L+1}$. Subsequently, J_{L+1} may be expressed as

$$J_{L+1} = a + \sum_{j=1}^{N_L-1} (\epsilon_{L_j} - \mu_L)^2. \quad (39)$$

The second term in J_L may be expressed as

$$\begin{aligned} \sum_{j=1}^{N_L} (\epsilon_{L_j} - \mu_L)^2 &= \sum_{j=1}^{N_L} \epsilon_{L_j}^2 - N_L \mu_L^2 \\ &= \sum_{j=1}^{N_L-1} \epsilon_{L_j}^2 - N_L \mu_L^2 + \epsilon_{L_{N_L}}^2. \end{aligned} \quad (40)$$

The term $N_L \mu_L^2$ may be expressed as

$$\begin{aligned} N_L \mu_L^2 &= N_L \left(\frac{1}{N_L} \sum_{j=1}^{N_L} \epsilon_{L_j} \right)^2 \\ &= \frac{1}{N_L} \left(\sum_{j=1}^{N_L-1} \epsilon_{L_j} + \epsilon_{L_{N_L}} \right)^2 \\ &= \frac{1}{N_L} [(N_L - 1) \mu'_L + \epsilon_{L_{N_L}}]^2 \\ &= \frac{(N_L - 1)^2 \mu'^2_L}{N_L} + \frac{2(N_L - 1) \mu'_L \epsilon_{L_{N_L}}}{N_L} + \frac{\epsilon_{L_{N_L}}^2}{N_L} \\ &= (N_L - 1) \mu'^2_L - \frac{(N_L - 1) \mu'^2_L}{N_L} \\ &\quad + \frac{2(N_L - 1) \mu'_L \epsilon_{L_{N_L}}}{N_L} + \frac{\epsilon_{L_{N_L}}^2}{N_L} + \epsilon_{L_{N_L}}^2 - \epsilon_{L_{N_L}}^2 \\ &= (N_L - 1) \mu'^2_L - \frac{(N_L - 1)}{N_L} (\epsilon_{L_{N_L}} - \mu'_L)^2 + \epsilon_{L_{N_L}}^2. \end{aligned} \quad (41)$$

Substituting back in the second term of J_L yields

$$\begin{aligned} & \sum_{j=1}^{N_L} (\epsilon_{L_j} - \mu_L)^2 \\ &= \sum_{j=1}^{N_L-1} (\epsilon_{L_j} - \mu'_L)^2 + \frac{(N_L - 1)}{N_L} (\epsilon_{L_{N_L}} - \mu'_L)^2. \end{aligned} \quad (42)$$

Substituting back in J_L yields

$$\begin{aligned} J_L &= a + \sum_{j=1}^{N_L-1} (\epsilon_{L_j} - \mu'_L)^2 + \frac{(N_L - 1)}{N_L} (\epsilon_{L_{N_L}} - \mu'_L)^2 \\ &= J_{L+1} + \frac{(N_L - 1)}{N_L} (\epsilon_{L_{N_L}} - \mu'_L)^2. \end{aligned} \quad (43)$$

Since $\frac{(N_L-1)}{N_L} (\epsilon_{L_{N_L}} - \mu'_L)^2 \geq 0$, then $J_L \geq J_{L+1}$. \square

APPENDIX C PROOF OF THEOREM III.3

This appendix provides the proof of Theorem III.3 stating that adding a carrier phase measurement from an additional cellular SOP while augmenting the clock state vector $c\delta t$ by its corresponding additional clock state will neither change the position error nor the position error uncertainty.

PROOF: The augmented Jacobian matrix is given by

$$\mathbf{H}' = \begin{bmatrix} \mathbf{G} & \mathbf{\Gamma} & \mathbf{0} \\ \mathbf{g}^T & \mathbf{0}^T & 1 \end{bmatrix} \quad (44)$$

where $\mathbf{g} \triangleq \frac{\hat{\mathbf{r}}_r - \mathbf{r}_{s_{N+1}}}{\sqrt{\|\hat{\mathbf{r}}_r - \mathbf{r}_{s_{N+1}}\|_2^2 + \Delta z_{r,s_{N+1}}^2}}$. The new information matrix is subsequently given by

$$\mathbf{H}'^T \mathbf{H}' = \begin{bmatrix} \mathbf{G}^T \mathbf{G} + \mathbf{g} \mathbf{g}^T & \mathbf{G}^T \mathbf{\Gamma} & \mathbf{g} \\ \mathbf{\Gamma}^T \mathbf{G} & \mathbf{\Gamma}^T \mathbf{\Gamma} & \mathbf{0} \\ \mathbf{g}^T & \mathbf{0}^T & 1 \end{bmatrix} = \begin{bmatrix} \mathbf{M}_{11} & \mathbf{m}_{12} \\ \mathbf{m}_{12}^T & 1 \end{bmatrix} \quad (45)$$

where

$$\mathbf{M}_{11} \triangleq \begin{bmatrix} \mathbf{G}^T \mathbf{G} + \mathbf{g} \mathbf{g}^T & \mathbf{G}^T \mathbf{\Gamma} \\ \mathbf{\Gamma}^T \mathbf{G} & \mathbf{\Gamma}^T \mathbf{\Gamma} \end{bmatrix}, \mathbf{m}_{12} \triangleq \begin{bmatrix} \mathbf{g} \\ \mathbf{0} \end{bmatrix}.$$

The new covariance is given by

$$\mathbf{P}' = (\mathbf{H}'^T \mathbf{H}')^{-1} = \begin{bmatrix} \mathbf{A}' & \mathbf{b}' \\ \mathbf{b}'^T & d' \end{bmatrix} \quad (46)$$

where

$$\begin{aligned} \mathbf{A}' &= (\mathbf{M}_{11} - \mathbf{m}_{12} \mathbf{m}_{12}^T)^{-1} \\ \mathbf{b}' &= -(\mathbf{M}_{11} - \mathbf{m}_{12} \mathbf{m}_{12}^T)^{-1} \mathbf{m}_{12} \\ d' &= 1 + \mathbf{m}_{12}^T (\mathbf{M}_{11} - \mathbf{m}_{12} \mathbf{m}_{12}^T)^{-1} \mathbf{m}_{12}. \end{aligned}$$

The matrix \mathbf{A}' may be expressed as

$$\begin{aligned} \mathbf{A}' &= \left(\begin{bmatrix} \mathbf{G}^T \mathbf{G} + \mathbf{g} \mathbf{g}^T & \mathbf{G}^T \mathbf{\Gamma} \\ \mathbf{\Gamma}^T \mathbf{G} & \mathbf{\Gamma}^T \mathbf{\Gamma} \end{bmatrix} - \begin{bmatrix} \mathbf{g} \mathbf{g}^T & \mathbf{0} \\ \mathbf{0}^T & \mathbf{0} \end{bmatrix} \right)^{-1} \\ &= \begin{bmatrix} \mathbf{G}^T \mathbf{G} & \mathbf{G}^T \mathbf{\Gamma} \\ \mathbf{\Gamma}^T \mathbf{G} & \mathbf{\Gamma}^T \mathbf{\Gamma} \end{bmatrix}^{-1} = \mathbf{P} \end{aligned} \quad (47)$$

which indicates that the new uncertainty in the position state is unchanged. The new covariance can be expressed as

$$\mathbf{P}' = \begin{bmatrix} \mathbf{P} & -\mathbf{P} \mathbf{m}_{12} \\ -\mathbf{m}_{12}^T \mathbf{P} & 1 + \mathbf{m}_{12}^T \mathbf{P} \mathbf{m}_{12} \end{bmatrix} = \begin{bmatrix} \mathbf{P}'_{11} & \mathbf{P}'_{12} & \mathbf{P}'_{13} \\ \mathbf{P}'_{12}^T & \mathbf{P}'_{22} & \mathbf{P}'_{23} \\ \mathbf{P}'_{13}^T & \mathbf{P}'_{23}^T & \mathbf{P}'_{33} \end{bmatrix} \quad (48)$$

where

$$\begin{aligned} \mathbf{P}'_{11} &= (\mathbf{G}^T \mathbf{\Psi} \mathbf{G})^{-1} \\ \mathbf{P}'_{12} &= -(\mathbf{G}^T \mathbf{\Psi} \mathbf{G})^{-1} \mathbf{G}^T \mathbf{\Gamma} (\mathbf{\Gamma}^T \mathbf{\Gamma})^{-1} \\ \mathbf{P}'_{13} &= -(\mathbf{G}^T \mathbf{\Psi} \mathbf{G})^{-1} \mathbf{g} \\ \mathbf{P}'_{22} &= (\mathbf{\Gamma}^T \mathbf{\Gamma})^{-1} \mathbf{\Gamma}^T [\mathbf{I} + \mathbf{G} (\mathbf{G}^T \mathbf{\Psi} \mathbf{G})^{-1} \mathbf{G}^T] \mathbf{\Gamma} (\mathbf{\Gamma}^T \mathbf{\Gamma})^{-1} \\ \mathbf{P}'_{23} &= (\mathbf{\Gamma}^T \mathbf{\Gamma})^{-1} \mathbf{\Gamma}^T \mathbf{G} (\mathbf{G}^T \mathbf{\Psi} \mathbf{G})^{-1} \mathbf{g} \\ \mathbf{P}'_{33} &= 1 + \mathbf{g}^T (\mathbf{G}^T \mathbf{\Psi} \mathbf{G})^{-1} \mathbf{g}. \end{aligned}$$

The new estimation error is given by

$$\delta \mathbf{r}'_r(k) = -\mathbf{P}' \mathbf{H}'^T \boldsymbol{\epsilon}'(k) \quad (49)$$

where $\boldsymbol{\epsilon}'(k) \triangleq [\boldsymbol{\epsilon}^T(k), \epsilon_{N+1}(k)]^T$ and $\epsilon_{N+1}(k)$ is the error from the $(N+1)^{\text{st}}$ measurement. Using the expressions of \mathbf{P}' , \mathbf{H}' , and $\boldsymbol{\epsilon}'$, it can be readily shown that

$$\delta \mathbf{r}'_r(k) = -(\mathbf{G}^T \mathbf{\Psi} \mathbf{G})^{-1} \mathbf{G}^T \mathbf{\Psi} \boldsymbol{\epsilon}(k) = \delta \mathbf{r}_r(k). \quad (50)$$

Therefore, the addition of a measurement while augmenting the clock state vector by one state will not improve the position estimate nor the position error uncertainty. \square

APPENDIX D

Table of ARMA Coefficients for Experiment 1

BTS	AR coefficients	MA coefficients	$\sigma_{w\epsilon_n}$ (mm)
1	[1, -1.167, -0.023, -0.508, 0.743, 0.323, -0.363]	[1, -0.349, -0.399, -0.834, 0.0960, 0.406, 0.087]	3.1
2	[1, -1.596, 0.934, 0.132, -0.826, 0.508, -0.035]	[1, -0.692, 0.224, 0.328, -0.485, -0.073, 0.004]	2.5
3	[1, -1.052, -0.407, 0.356, -0.121, 0.588, -0.352]	[1, -0.368, -0.657, -0.240, -0.208, 0.525, -0.011]	3.6
4	[1, -0.208, -0.512, 0.506, -0.564, -0.340, 0.5742]	[1, 0.439, -0.203, 0.388, -0.417, -0.626, 0.161]	2.9
5	[1, -1.06, 0.006, -0.484, 0.596, 0.329, -0.331]	[1, -0.250, -0.270, -0.771, -0.009, 0.402, -0.009]	2.9
6	[1, -2.350, 2.450, -1.750, 0.890, -0.243, 0.0419]	[1, -1.417, 1.062, -0.714, 0.212, -0.099, 0.103]	2.9
7	[1, -0.208, -0.512, 0.505, -0.564, -0.340, 0.574]	[1, 0.43, -0.203, 0.388, -0.417, -0.626, 0.161]	2.9
8	[1, 0.835, -0.656, -0.629, -0.028, 0.270, 0.221]	[1, 1.569, 0.484, -0.350, -0.383, -0.005, 0.146]	3.3
9	[1, 0.134, -0.450, 0.518, -0.427, -0.391, 0.468]	[1, 0.995, 0.230, 0.552, 0.0380, -0.608, -0.128]	57.5

ACKNOWLEDGMENT

The authors would like to thank Joshua Morales, Kimia Shamaei, and Mahdi Maaref for their help in data collection.

REFERENCES

- [1] R. Loh, Y. Bia, and T. Roe
UAVs in civil airspace: Safety requirement
IEEE Aerosp. Electron. Syst. Mag., vol. 24, no. 1, pp. 5–17, Jan. 2009.

- [2] A. Kerns, D. Shepard, J. Bhatti, and T. Humphreys
Unmanned aircraft capture and control via GPS spoofing
J. Field Robot., vol. 31, no. 4, pp. 617–636, 2014.
- [3] D. Borio, F. Dovis, H. Kuusniemi, and L. Presti
Impact and detection of GNSS jammers on consumer grade satellite navigation receivers
Proc. IEEE, vol. 104, no. 6, pp. 1233–1245, Jun. 2016.
- [4] N. Kbayer and M. Sahnoudi
Performances analysis of GNSS NLOS bias correction in urban environment using a threedimensional city model and GNSS simulator
IEEE Trans. Aerosp. Electron. Syst., vol. 54, no. 4, pp. 1799–1814, Aug. 2018.
- [5] J. McEllroy
Navigation using signals of opportunity in the AM transmission band
M.S. thesis, Air Force Inst. of Technol., Wright-Patterson Air Force Base, OH, USA, 2006.
- [6] V. Moghtadaiee and A. Dempster
Indoor location fingerprinting using FM radio signals
IEEE Trans. Broadcast., vol. 60, no. 2, pp. 336–346, Jun. 2014.
- [7] X. Chen, Q. Wei, F. Wang, Z. Jun, S. Wu, and A. Men
Super-resolution time of arrival estimation for a symbiotic FM radio data system
IEEE Trans. Broadcast., vol. 66, no. 4, pp. 847–856, Dec. 2020.
- [8] T. Reid, A. Neish, T. Walter, and P. Enge
Broadband LEO constellations for navigation
NAVIGATION, J. Inst. Navig., vol. 65, no. 2, pp. 205–220, 2018.
- [9] J. Khalife, M. Neinavaie, and Z. Kassas
Navigation with differential carrier phase measurements from megaconstellation LEO satellites
In *Proc. IEEE/ION Position, Location, Navig. Symp.*, 2020, pp. 1393–1404.
- [10] F. Farhangian and R. Landry
Multi-constellation software-defined receiver for Doppler positioning with LEO satellites
Sensors, vol. 20, no. 20, pp. 5866–5883, Oct. 2020.
- [11] F. Farhangian, H. Benzerrouk, and R. Landry
Opportunistic in-flight INS alignment using LEO satellites and a rotatory IMU platform
Aerospace, vol. 8, no. 10, pp. 280–281, 2021.
- [12] Z. Kassas *et al.*
Enter LEO on the GNSS stage: Navigation with Starlink satellites
Inside GNSS Mag., vol. 16, no. 6, pp. 42–51, 2021.
- [13] N. Chang, R. Rashidzadeh, and M. Ahmadi
Robust indoor positioning using differential Wi-Fi access points
IEEE Trans. Consum. Electron., vol. 56, no. 3, pp. 1860–1867, Aug. 2010.
- [14] R. Faragher, C. Sarno, and M. Newman
Opportunistic radio SLAM for indoor navigation using smartphone sensors
In *Proc. IEEE/ION Position Location Navigation Symp.*, 2012, pp. 120–128.
- [15] I. Bisio *et al.*
A trainingless WiFi fingerprint positioning approach over mobile devices
IEEE Antennas Wireless Propag. Lett., vol. 13, pp. 832–835, 2014.
- [16] Y. Zhuang and N. El-Sheimy
Tightly-coupled integration of WiFi and MEMS sensors on handheld devices for indoor pedestrian navigations
IEEE Sensors J., vol. 16, no. 1, pp. 224–234, Jan. 2016.
- [17] M. Rabinowitz and J. Spilker
The rosum television positioning technolog
In *Proc. Annu. Meeting Inst. Navigation CIGTF Guid. Test Symp.*, 2003, pp. 528–541.
- [18] P. Thevenon *et al.*
Positioning using mobile TV based on the DVB-SH standard
J. Inst. Navigation, vol. 58, no. 2, pp. 71–90, 2011.
- [19] J. Yang, X. Wang, M. Rahman, S. Park, H. Kim, and Y. Wu
A new positioning system using DVB-T2 transmitter signature waveforms in single frequency networks
IEEE Trans. Broadcast., vol. 58, no. 3, pp. 347–359, Sep. 2012.
- [20] L. Chen, O. Julien, P. Thevenon, D. Serant, A. Pena, and H. Kuusniemi
TOA estimation for positioning with DVB-T signals in outdoor static tests
IEEE Trans. Broadcast., vol. 61, no. 4, pp. 625–638, Dec. 2015.
- [21] C. Yang and A. Soloviev
Mobile positioning with signals of opportunity in urban and urban canyon environments
In *Proc. IEEE/ION Position, Location, Navigation Symp.*, 2020, pp. 1043–1059.
- [22] C. Yang and T. Nguyen
Tracking and relative positioning with mixed signals of opportunity
J. Inst. Navig., vol. 62, no. 4, pp. 291–311, Dec. 2015.
- [23] K. Shamaei, J. Khalife, and Z. Kassas
Exploiting LTE signals for navigation: Theory to implementation
IEEE Trans. Wireless Commun., vol. 17, no. 4, pp. 2173–2189, Apr. 2018.
- [24] J. Khalife and Z. Kassas
Navigation with cellular CDMA signals — Part II: Performance analysis and experimental results
IEEE Trans. Signal Process., vol. 66, no. 8, pp. 2204–2218, Apr. 2018.
- [25] J. Khalife and Z. Kassas
Precise UAV navigation with cellular carrier phase measurements
In *Proc. IEEE/ION Position, Location, Navig. Symp.*, 2018, pp. 978–989.
- [26] J. del Peral-Rosado, R. Raulefs, J. López-Salcedo, and G. Seco-Granados
Survey of cellular mobile radio localization methods: From 1G to 5G
IEEE Commun. Surv. Tut., vol. 20, no. 2, pp. 1124–1148, Apr.–Jun. 2018.
- [27] E. Kim and Y. Shin
Feasibility analysis of LTE-based UAS navigation in deep urban areas and DSRC augmentation
Sensors, vol. 19, no. 9, pp. 4192–4207, Apr. 2019.
- [28] T. Kang, H. Lee, and J. Seo
TOA-based ranging method using CRS in LTE signals
J. Adv. Navig. Technol., vol. 23, no. 5, pp. 437–443, Oct. 2019.
- [29] C. Yang, T. Pany, and P. Weitkemper
Effect of antenna ports on TOA estimation with 4G LTE signals in urban mobile environments
In *Proc. ION Int. Tech. Meeting Conf.*, 2020, pp. 2166–2181.
- [30] J. Mortier, G. Pages, and J. Vila-Valls
Robust TOA-based UAS navigation under model mismatch in GNSS-denied harsh environments
Remote Sens., vol. 12, no. 18, pp. 2928–2947, Sep. 2020.
- [31] H. Dun, C. Tiberius, and G. Janssen
Positioning in a multipath channel using OFDM signals with carrier phase tracking
IEEE Access, vol. 8, pp. 13011–13028, 2020.
- [32] J. Gante, L. Sousa, and G. Falcao
Dethroning GPS: Low-power accurate 5G positioning systems using machine learning
IEEE Trans. Emerg. Sel. Topics Circuits Syst., vol. 10, no. 2, pp. 240–252, Jun. 2020.
- [33] C. Gentner, T. Jost, W. Wang, S. Zhang, A. Dammann, and U. Fiebig
Multipath assisted positioning with simultaneous localization and mapping

- IEEE Trans. Wireless Commun.*, vol. 15, no. 9, pp. 6104–6117, Sep. 2016.
- [34] P. Muller, J. del Peral-Rosado, R. Piche, and G. Seco-Granados
Statistical trilateration with skew-t distributed errors in LTE networks
IEEE Trans. Wireless Commun., vol. 15, no. 10, pp. 7114–7127, Oct. 2016.
- [35] M. Driusso, C. Marshall, M. Sabathy, F. Knutti, H. Mathis, and F. Babich
Vehicular position tracking using LTE signals
IEEE Trans. Veh. Technol., vol. 66, no. 4, pp. 3376–3391, Apr. 2017.
- [36] Z. Kassas, J. Morales, K. Shamaei, and J. Khalife
LTE steers UAV
GPS World Mag., vol. 28, no. 4, pp. 18–25, Apr. 2017.
- [37] K. Shamaei and Z. Kassas
LTE receiver design and multipath analysis for navigation in urban environments
J. Inst. Navig., vol. 65, no. 4, pp. 655–675, Dec. 2018.
- [38] Z. Kassas, M. Maaref, J. Morales, J. Khalife, and K. Shamaei
Robust vehicular localization and map matching in urban environments through IMU, GNSS, and cellular signals
IEEE Intell. Transp. Syst. Mag., vol. 12, no. 3, pp. 36–52, Jun. 2020.
- [39] N. Souli, P. Kolios, and G. Ellinas
Online relative positioning of autonomous vehicles using signals of opportunity
IEEE Trans. Intell. Veh., to be published, doi: [10.1109/TIV.2021.3124727](https://doi.org/10.1109/TIV.2021.3124727).
- [40] G. Retscher, H. Hofer, A. Kealy, V. Gikas, and F. Obex
Cooperative localization in indoor environments using constrained differential Wi-Fi and UWB measurements
In Proc. 30th Int. Tech. Meeting Satell. Division Inst. Navigation Conf., 2017, pp. 2869–2882.
- [41] T. Zhao, K. Zhao, C. Yu, D. Dong, Z. Zheng, and Y. Zhang
Application of differential time synchronization in indoor positioning
In Proc. Int. Conf. Wireless Commun. Signal Process., 2019, pp. 1–6.
- [42] J. del Peral-Rosado *et al.*
Software-defined radio LTE positioning receiver towards future hybrid localization systems
In Proc. Int. Commun. Satell. Syst. Conf., 2013, pp. 1–11.
- [43] C. Yang, T. Nguyen, and E. Blasch
Mobile positioning via fusion of mixed signals of opportunity
IEEE Aerosp. Electron. Syst. Mag., vol. 29, no. 4, pp. 34–46, Apr. 2014.
- [44] J. Khalife, K. Shamaei, and Z. Kassas
Navigation with cellular CDMA signals - Part I: Signal modeling and software-defined receiver design
IEEE Trans. Signal Process., vol. 66, no. 8, pp. 2191–2203, Apr. 2018.
- [45] K. Shamaei and Z. Kassas
Receiver design and time of arrival estimation for opportunistic localization with 5G signals
IEEE Trans. Wireless Commun., vol. 20, no. 7, pp. 4716–4731, Jul. 2021.
- [46] M. Lichtman, R. Jover, M. Labib, R. Rao, V. Marojevic, and J. Reed
LTE/LTE-A jamming, spoofing, and sniffing: Threat assessment and mitigation
IEEE Commun. Mag., vol. 54, no. 4, pp. 54–61, Apr. 2016.
- [47] M. Lichtman, R. Rao, V. Marojevic, J. Reed, and R. Jover
5G NR jamming, spoofing, and sniffing: Threat assessment and mitigation
In Proc. IEEE Int. Conf. Commun. Workshops, 2018, pp. 1–6.
- [48] A. Gupta, R. Jha, P. Gandotra, and S. Jain
Bandwidth spoofing and intrusion detection system for multi-stage 5G wireless communication network
IEEE Trans. Veh. Technol., vol. 67, no. 1, pp. 618–632, Jan. 2018.
- [49] W. Xu, C. Yuan, S. Xu, H. Ngo, and W. Xiang
On pilot spoofing attack in massive MIMO systems: Detection and countermeasure
IEEE Trans. Inf. Forensics Secur., vol. 16, pp. 1396–1409, 2021.
- [50] A. Abdallah, J. Khalife, and Z. Kassas
Experimental characterization of received 5G signals carrier-to-noise ratio in indoor and urban environments
In Proc. IEEE Veh. Technol. Conf., 2021, pp. 1–5.
- [51] J. Khalife, K. Shamaei, S. Bhattacharya, and Z. Kassas
Centimeter-accurate UAV navigation with cellular signals
In Proc. 31st Int. Techn. Meeting Satell. Division Inst. Navigation Conf., 2018, pp. 2321–2331.
- [52] Z. Kassas
Analysis and synthesis of collaborative opportunistic navigation systems
Ph.D. dissertation, University of Texas, Austin, TX, USA, 2014.
- [53] C. Yang and A. Soloviev
Simultaneous localization and mapping of emitting radio sources-SLAMERS
In Proc. 28th Int. Tech. Meeting Satell. Division Inst. Navigation Conf., 2015, pp. 2343–2354.
- [54] C. Gentner, B. Ma, M. Ulmschneider, T. Jost, and A. Dammann
Simultaneous localization and mapping in multipath environments
In Proc. IEEE/ION Position Location Navigation Symp., 2016, pp. 807–815.
- [55] J. Morales and Z. Kassas
Tightly-coupled inertial navigation system with signals of opportunity aiding
IEEE Trans. Aerosp. Electron. Syst., vol. 57, no. 3, pp. 1930–1948, Jun. 2021.
- [56] J. Morales and Z. Kassas
Optimal collaborative mapping of terrestrial transmitters: Receiver placement and performance characterization
IEEE Trans. Aerosp. Electron. Syst., vol. 54, no. 2, pp. 992–1007, Apr. 2018.
- [57] Z. Kassas, J. Khalife, A. Abdallah, and C. Lee
I am not afraid of the jammer: Navigating with signals of opportunity in GPS-denied environments
In Proc. 33rd Int. Tech. Meeting Satell. Division Inst. Navigation Conf., 2020, pp. 1566–1585.
- [58] *Physical Layer Standard for CDMA2000 Spread Spectrum Systems (C.S0002-E)*, 3GPP2, 3rd Generation Partnership Project 2 (3GPP2), TS C.S0002-E, Jun. 2011.
- [59] *Evolved Universal Terrestrial Radio Access (E-UTRA); Physical Channels and Modulation*, 3GPP, 3rd Generation Partnership Project (3GPP), TS 36.211, Jan. 2011. [Online]. Available: <http://www.3gpp.org/ftp/Specs/html-info/36211.htm>
- [60] M. Ulmschneider and C. Gentner
Multipath assisted positioning for pedestrians using LTE signals
In Proc. IEEE/ION Position, Location, Navigation Symp., 2016, pp. 386–392.
- [61] P. Misra and P. Enge
Global Positioning System: Signals, Measurements, and Performance, 2nd ed. Lincoln, MA, USA: Ganga-Jamuna Press, 2010.
- [62] M. Maaref and Z. Kassas
Measurement characterization and autonomous outlier detection and exclusion for ground vehicle navigation with cellular signals
IEEE Trans. Intell. Veh., vol. 5, no. 4, pp. 670–683, Dec. 2020.
- [63] S. Ragothaman, M. Maaref, and Z. Kassas
Autonomous ground vehicle path planning in urban environments using GNSS and cellular signals reliability maps: Models and algorithms
IEEE Trans. Aerosp. Electron. Syst., vol. 57, no. 2, pp. 1562–1580, Jun. 2021.
- [64] M. Maaref, J. Khalife, and Z. Kassas
Aerial vehicle protection level reduction by fusing GNSS and

- terrestrial signals of opportunity
IEEE Trans. Intell. Transp. Syst., vol. 22, no. 9, pp. 5976–5993, Sep. 2021.
- [65] Qualcomm Technologies, Inc. LTE unmanned aircraft systems Tech. Rep. 1.0.1, May 2017. [Online]. Available: <https://www.qualcomm.com/documents/lte-unmanned-aircraft-systems-trial-report/>
- [66] X. Chen, F. Dovis, and M. Pini
An innovative multipath mitigation method using coupled amplitude delay lock loops in GNSS receivers
In *Proc. IEEE/ION Position, Location, Navigation Symp.*, 2010, pp. 1118–1126.
- [67] O. Bialer, D. Raphaeli, and A. Weiss
Efficient time of arrival estimation algorithm achieving maximum likelihood performance in dense multipath
IEEE Trans. Signal Process., vol. 60, no. 3, pp. 1241–1252, Mar. 2012.
- [68] J. del Peral-Rosado, J. López-Salcedo, F. Zanier, and G. Seco-Granados
Position accuracy of joint time-delay and channel estimators in LTE networks
IEEE Access, vol. 6, pp. 25185–25199, 2018.
- [69] Y. Quan, L. Lau, G. Roberts, X. Meng, and C. Zhang
Convolutional neural network based multipath detection method for static and kinematic GPS high precision positioning
Remote Sens., vol. 10, no. 12, Dec. 2018, Art. no. 2052.
- [70] P. Wang and Y. Morton
Performance comparison of time-of-arrival estimation techniques for LTE signals in realistic multipath propagation channels
NAVIGATION, J. Inst. Navigation, vol. 67, no. 4, pp. 691–712, Dec. 2020.
- [71] P. Wang and Y. Morton
Multipath estimating delay lock loop for LTE signal TOA estimation in indoor and urban environments
IEEE Trans. Wireless Commun., vol. 19, no. 8, pp. 5518–5530, Aug. 2020.
- [72] A. Abdallah and Z. Kassas
Multipath mitigation via synthetic aperture beamforming for indoor and deep urban navigation
IEEE Trans. Veh. Technol., vol. 70, no. 9, pp. 8838–8853, Sep. 2021.
- [73] M. Joerger and B. Pervan
Fault detection and exclusion using solution separation and chi-squared ARAIM
IEEE Trans. Aerosp. Electron. Syst., vol. 52, no. 2, pp. 726–742, Apr. 2016.
- [74] N. Zhu, J. Marais, D. Betaille, and M. Berbineau
GNSS position integrity in urban environments: A review of literature
IEEE Trans. Intell. Transp. Syst., vol. 19, no. 9, pp. 2762–2778, Sep. 2018.
- [75] N. Zhu, D. Betaille, J. Marais, and M. Berbineau
GNSS integrity monitoring schemes for terrestrial applications in harsh signal environments
IEEE Intell. Transp. Syst. Mag., vol. 12, no. 3, pp. 81–91, Mar. 2020.
- [76] N. Ziedan
Multipath channel estimation and pattern recognition for environment-based adaptive tracking
In *Proc. 25th Int. Tech. Meeting Satell. Division Inst. Navigation Conf.*, 2012, pp. 394–407.
- [77] Y. Wang, X. Chen, and P. Liu
Statistical multipath model based on experimental GNSS data in static urban canyon environment
Sensors, vol. 18, no. 4, Apr. 2018, Art. no. 1149.
- [78] J. Khalife and Z. Kassas
Evaluation of relative clock stability in cellular networks
In *Proc. 30th Int. Tech. Meeting Satell. Division Inst. Navigation Conf.*, 2017, pp. 2554–2559.
- [79] J. Khalife and Z. Kassas
Opportunistic UAV navigation with carrier phase measurements from asynchronous cellular signals
IEEE Trans. Aerosp. Electron. Syst., vol. 56, no. 4, pp. 3285–3301, Aug. 2020.
- [80] J. Morales and Z. Kassas
Stochastic observability and uncertainty characterization in simultaneous receiver and transmitter localization
IEEE Trans. Aerosp. Electron. Syst., vol. 55, no. 2, pp. 1021–1031, Apr. 2019.
- [81] L. Ljung
System Identification: Theory for the User. 2nd ed. Englewood Cliffs, NJ, USA: Prentice-Hall, 1999.
- [82] J. Khalife, C. Sevinc, and Z. Kassas
Performance evaluation of TOA positioning in asynchronous cellular networks using stochastic geometry models
IEEE Wireless Commun. Lett., vol. 9, no. 9, pp. 1422–1426, Sep. 2020.
- [83] J. Wirth, E. Bonugli, and M. Freund
Assessment of the accuracy of Google Earth imagery for use as a tool in accident reconstruction
In *Proc. SAE World Congr. Exhib.*, 2015, pp. 1–17.
- [84] C. Yang and T. Nguyen
Self-calibrating position location using signals of opportunity
In *Proc. 22nd Int. Tech. Meeting Satell. Division Inst. Navigation Conf.*, 2009, pp. 1055–1063.



Joe Khalife (Member, IEEE) received the B.E. degree in electrical engineering and the M.S. degree in computer engineering from the Lebanese American University (LAU), Beirut, Lebanon, in 2011 and 2014, respectively and the Ph.D. degree in electrical engineering and computer science from the University of California, Irvine, CA, USA, in 2020.

He is a Postdoctoral Fellow with the University of California, Irvine and member of the Autonomous Systems Perception, Intelligence, and Navigation (ASPIN) Laboratory. From 2012 to 2015, he was a Research Assistant with LAU, and has been a member of the ASPIN Laboratory since 2015. His research interests include opportunistic navigation, autonomous vehicles, and software-defined radio.

Dr. Khalife is a recipient of the 2016 IEEE/ION Position, Location, and Navigation Symposium (PLANS) Best Student Paper Award and the 2018 IEEE Walter Fried Award.



Zaher M. Kassas (Senior Member, IEEE) received the B.E. degree in electrical engineering from the Lebanese American University, Beirut, Lebanon, the M.S. degree in electrical and computer engineering from The Ohio State University, Columbus, OH, USA, and the M.S.E. degree in aerospace engineering and the Ph.D. degree in electrical and computer engineering from The University of Texas at Austin, Austin, TX, USA.

He is currently an Associate Professor with the University of California, Irvine, CA, USA, and the Director of the Autonomous Systems Perception, Intelligence, and Navigation (ASPIN) Laboratory. He is also the Director of the U.S. Department of Transportation Center: CARMEN (Center for Automated Vehicle Research with Multimodal Assured Navigation), focusing on navigation resiliency and security of highly automated transportation systems. His research interests include cyber-physical systems, estimation theory, navigation systems, autonomous vehicles, and intelligent transportation systems.

Prof. Kassas is a recipient of the 2018 National Science Foundation (NSF) Faculty Early Career Development Program (CAREER) award, 2019 Office of Naval Research (ONR) Young Investigator Program (YIP) award, 2022 Air Force Office of Scientific Research (AFOSR) YIP award, 2018 IEEE Walter Fried Award, 2018 Institute of Navigation (ION) Samuel Burka Award, and 2019 ION Col. Thomas Thurlow Award. He is a Senior Editor of the IEEE TRANSACTIONS ON INTELLIGENT VEHICLES and an Associate Editor of the IEEE TRANSACTIONS ON AEROSPACE AND ELECTRONIC SYSTEMS and the IEEE TRANSACTIONS ON INTELLIGENT TRANSPORTATION SYSTEMS.